Matrix Biology 128 (2024) 39–64

Contents lists available at ScienceDirect

Matrix Biology

journal homepage: www.elsevier.com/locate/matbio

Microvascular damage, neuroinflammation and extracellular matrix remodeling in *Col18a1* knockout mice as a model for early cerebral small vessel disease

Mahsima Khoshneviszadeh [a,b], Solveig Henneicke [a,b], Daniel Pirici [c], Akilashree Senthilnathan [a], Lorena Morton [d], Philipp Arndt [a,b], Rahul Kaushik [a], Oula Norman [e], Jari Jukkola [e], Ildiko Rita Dunay [d,f,h], Constanze Seidenbecher [f,g,h], Anne Heikkinen [e], Stefanie Schreiber [a,b,f,h,*], Alexander Dityatev [a,f,i,*]

[a] German Center for Neurodegenerative Diseases (DZNE), Magdeburg, Germany
[b] Department of Neurology, Otto-von-Guericke University, Magdeburg, Germany
[c] Department of Histology, University of Medicine and Pharmacy of Craiova, Craiova, Romania
[d] Institute of Inflammation and Neurodegeneration, Medical Faculty, Otto-von-Guericke University, Magdeburg, Germany
[e] Faculty of Biochemistry and Molecular Medicine, University of Oulu, Finland
[f] Center for Behavioral Brain Sciences (CBBS), Magdeburg, Germany
[g] Leibniz Institute for Neurobiology, Magdeburg, Germany
[h] Center for Intervention and Research on Adaptive and Maladaptive Brain Circuits Underlying Mental Health (C-I-R-C), Jena-Magdeburg-Halle, Germany
[i] Medical Faculty, Otto-von-Guericke University, Magdeburg, Germany

ARTICLE INFO

Declarations

Keywords:
Small vessel disease
Extracellular matrix
Neuroinflammation
Microglia
Collagen XVIII
TIMP-3
Brevican

ABSTRACT

Collagen type XVIII (COL18) is an abundant heparan sulfate proteoglycan in vascular basement membranes. Here, we asked (i) if the loss of COL18 would result in blood-brain barrier (BBB) breakdown, pathological alterations of small arteries and capillaries and neuroinflammation as found in cerebral small vessel disease (CSVD) and (ii) if such changes may be associated with remodeling of synapses and neural extracellular matrix (ECM). We found that 5-month-old *Col18a1*$^{-/-}$ mice had elevated BBB permeability for mouse IgG in the deep gray matter, and intravascular erythrocyte accumulations were observed brain-wide in capillaries and arterioles. BBB permeability increased with age and affected cortical regions and the hippocampus in 12-month-old *Col18a1*$^{-/-}$ mice. None of the *Col18a1*$^{-/-}$ mice displayed hallmarks of advanced CSVD, such as hemorrhages, and did not show perivascular space enlargement. *Col18a1* deficiency-induced BBB leakage was accompanied by activation of microglia and astrocytes, a loss of aggrecan in the ECM of perineuronal nets associated with fast-spiking inhibitory interneurons and accumulation of the perisynaptic ECM proteoglycan brevican and the microglial complement protein C1q at excitatory synapses. As the pathway underlying these regulations, we found increased signaling through the TGF-ß1/Smad3/TIMP-3 cascade. We verified the pivotal role of COL18 for small vessel wall structure in CSVD by demonstrating the protein's involvement in vascular remodeling in autopsy brains from patients with cerebral hypertensive arteriopathy. Our study highlights an association between the alterations of perivascular ECM, extracellular proteolysis, and perineuronal/perisynaptic ECM, as a possible substrate of synaptic and cognitive alterations in CSVD.

List of abbreviations

Abbreviation	Full name
Acan	Aggrecan
AD	Alzheimer's disease
Aqp4	Aquaporin 4
BBB	Blood-brain barrier
Bcan	Brevican
BG	Basal ganglia
C1q	Complement component 1q

* Corresponding authors at: German Center for Neurodegenerative Diseases (DZNE), Leipziger Str. 44, Haus 64, 39120 Magdeburg, Germany.
E-mail addresses: stefanie.schreiber@med.ovgu.de (S. Schreiber), alexander.dityatev@dzne.de (A. Dityatev).

https://doi.org/10.1016/j.matbio.2024.02.007
Received 26 April 2023; Received in revised form 17 February 2024; Accepted 19 February 2024
Available online 21 February 2024

CC	corpus callosum
Ccl2	Chemokine(C—C motif)ligand 2
CD86	Cluster of Differentiation 86
Cldn5	Claudin 5
CNS	Central nervous system
CSPG	Chondroitin sulfate proteoglycan
CSPG4	Chondroitin sulfate proteoglycan 4
CSVD	Cerebral small vessel disease
ECM	Extracellular matrix (ECM)
FOV	Fields of view
GFAP	Glial Fibrillary acidic protein
GWAS	Genome-wide association studies
Hapln1,2,3,4	Hyaluronan and proteoglycan link protein 1,2,3,4
Iba1	Ionized calcium-Binding Adapter molecule 1
IHC	Immunohistochemistry
IL-1β	Interleukin 1 beta
IL-6	Interleukin 6
IL-33	Interleukin 33
Lama5	Laminin alpha 5
Loxl2	Lysyl oxidase homolog 2
MRI	Magnetic resonance imaging
Mpo	Myeloperoxidase
Ncan	Neurocan
Nid1	Nidogen 1
Ocln	Occludin
PBS	Phosphate-buffered saline
Pcan	Phosphocan
PDGFRb	Platelet derived growth factor receptor, beta polypeptide
PNN	Perineuronal nets
PV	Parvalbumin
PVS	Perivascular spaces
Plp1	Proteolipid protein 1
ROI	Region of interest
RT-qPCR	Reverse transcription-polymerase chain reaction
RSC	Retrosplenial cortex
S100a10	S100 calcium-binding protein A10
SHRSP	Spontaneously hypertensive stroke-prone rat
TN-R	Tenascin-R
TNFa	Tumor necrosis factor alpha
VaD	vascular dementia
VCAM1	Vascular cell adhesion protein 1
Vcan	Versican
VGLUT1,2	Vesicular glutamate transporter 1,2
VGAT	Vesicular GABA transporter
WMH	White matter hyperintensities
Zo1	Zonula occludens-1

Introduction

Cerebral small vessel disease (CSVD) refers to a syndrome of clinical and imaging findings resulting from pathological processes in the brain's microvasculature [1]. An increased prevalence of age-related CSVD accompanies the steady worldwide increase in life expectancy, affecting approximately 5 % of people aged 50 years and approximately everyone older than 90 years, leading to an extensive social and economic burden [2]. The presenting symptoms and clinical courses of CSVD, such as stroke, cognitive decline [3], gait disturbance [4], apathy [5], depression [6] and extrapyramidal symptoms [7], are highly variable. The reasons for that variability are largely unknown, and several factors are discussed to play a role, including variations in vascular injury (location, type, and extent), varying degrees of secondary neurodegeneration, resilience and resistance factors such as brain function and structure, and concomitant diseases [8].

The pathogenesis of CSVD probably evolves sequentially, with an increase in permeability of the blood-brain barrier (BBB) [9] as an early event, supposedly followed by enlargement of Virchow Robin spaces (perivascular spaces (PVS)), and – later on – by e.g., subcortical infarcts, lacunes and microbleeds, which can be detected through routine magnetic resonance imaging (MRI) sometimes at a clinically still silent disease stage [10,11]. Axonal injury, neuronal apoptosis, demyelination, and oligodendrocyte damage also occur during CSVD, leading to cerebral parenchyma damage – usually mirrored by white matter hyperintensities (WMH) in neuroimaging - which may manifest through heterogeneous neurological symptoms [12,13]. Advanced age and arterial hypertension are the most accepted risk factors of CSVD [14].

The existing literature suggests that vascular inflammation and endothelial dysfunction may be the driving force, i.e. initiating events, of CSVD via disruption of the BBB and can occur in the presence or absence of systemic inflammation [15]. So far, early event detection is not part of the clinical imaging routine and disease-specific biofluid biomarkers are still under development. Still, endothelial function and BBB integrity are well known to be modified by (systemically detectable) proinflammatory cytokines, including tumor necrosis factor α (TNF-α) and interleukin 1 beta (IL-1β), which regulate the expression of the tight junction (TJ) proteins occludin-1, claudin-5 and zona occludes 1 (ZO-1), actin remodeling and changes in TJ structure [16,17]. Deeper profiling of markers and bystanders of endothelial dysfunction may provide new biomarkers for the early detection of initial stages of brain microvascular disease [14].

As there are currently no effective treatments or cures for CSVD, research on new animal models, biomarkers and (molecular) targets to uncover and ease the CSVD burden and predict its clinical course is of high scientific, clinical and socioeconomic relevance. Insights from transgenic animal models with mutations in genes encoding perivascular extracellular matrix (ECM) molecules [18], models with arterial hypertension [19], and human genome-wide association studies (GWAS) in CSVD [20] suggest that alterations in the (peri)vascular ECM are a pivotal part of the small vessel pathology. Therefore, alterations in basement membrane proteins, i.e., collagens, laminins, nidogens and perlecan, seem to be an underlying common mechanism [21–23]. Considering its regulatory roles in vascular remodeling, understanding the network of ECM-mediated interactions provides a series of potential therapeutic targets for vascular diseases. However, this regulatory network is still not completely understood [24].

Only a few animal models have been recognized to be suitable to study CSVD and its progression [25]. The spontaneously hypertensive stroke-prone rat (SHRSP) has been identified to be the most suitable one mimicking the inflammatory and degenerative small vessel changes and several associated lesions found in human CSVD so far [26]. As a multifactorial disease, CSVD is expected to have hereditary contributions from multiple genes, which need to be studied through the in-depth investigation of additional animal models.

Collagens constitute the most abundant ECM components in the vascular wall. Mutations, deficiencies, and other changes in collagen expression directly or indirectly affect the vasculature. Comprehensive clinical evidence indicates that COL4A1 mutations (Gly1236-to-Arg, Gly562-to-Glu) weaken the vessel wall of the overall arterial/arteriolar vasculature and cause recurrent cerebral and retinal microbleeds, WMH, retinal tortuosity, and lacunar infarcts in humans [27,28]. Furthermore, the relationship between COL3A1 and COL18A1 mutations and vessel fragility is well described in Ehlers-Danlos [29] and Knobloch syndromes [30,31], respectively.

COL18 is an abundant heparan sulfate proteoglycan in vascular and epithelial basement membranes [32]. It has been proposed that the triple-helical, heparan sulfate-containing portion of COL18 plays a role in the assembly, maintenance, structural integrity, or cellular binding properties of vascular basement membranes [33,34]. Based on these findings, we hypothesized that COL18, as a major component of the vascular basement membrane, has a vital role in the integrity of the small cerebral vasculature in mice and that loss of this vessel wall proteoglycan should be related to hallmark CSVD features, including increased BBB permeability. In this study, we also aimed to investigate

the potential role of ECM dysregulation in the pathogenesis of CSVD by examining changes in specific ECM components, matrix metalloproteinases and the tissue inhibitor of metalloproteinase 3 (TIMP-3), which has been reported to be upregulated in a preclinical model of and patients with genetic CSVD, i.e. cerebral autosomal dominant arteriopathy with subcortical infarcts and leukoencephalopathy (CADASIL) [35].

Our findings highlight vascular and neuroinflammatory alterations in *Col18a1* knockout (*Col18a1*$^{-/-}$) mice, which also appeared to result in abnormalities of excitatory synapses and associated perisynaptic and perineuronal ECM. Therefore, we not only suggest a new model for CSVD but also, for the first time, provide a link between small vessel, perineuronal and perisynaptic ECM alterations in CSVD. Our study also revealed that the upregulation of TIMP-3 and activation of the TGF-β1 signaling cascade were observed in the *Col18a1*$^{-/-}$ mice, which may contribute to the observed alterations in the ECM and associated vascular and synaptic abnormalities. These results highlight the importance of investigating the role of the ECM in the development of CSVD and generate new insights into potential therapeutic targets for this disorder.

Results

Erythrocyte aggregations, microbleeds, and PVS in Col18a1$^{-/-}$ *mice*

In a hypertensive rat model of CSVD, we have previously demonstrated that small vessels are affected by intravasal erythrocyte accumulations (stases) [26]. Hence, we examined HE-stained brain slices from 5- and 12-month-old mice. Similar to hypertensive rats, we found that the fraction of capillaries that displayed erythrocyte thrombi (Fig. 1 a, left) was significantly increased in 5-month-old *Col18a1*$^{-/-}$ mice compared to wild-type littermates (*Col18a1*$^{+/+}$) in all the brain regions studied, namely, the retrosplenial cortex (RSC: two-way ANOVA followed by Sidak's post hoc test; $p = 0.0078$), basal ganglia (BG: $p = 0.0099$), the CA1 region of the hippocampus (CA1: $p = 0.0011$), corpus callosum (CC: $p < 0.0001$) and the thalamus ($p = 0.0012$) (Fig. 1 b-f). For arterioles, there were similar increases in the occurrence of stases at this age in the RSC ($p = 0.0063$), BG ($p = 0.0025$), CA1 ($p = 0.0336$) and thalamus ($p = 0.0154$) but not in the CC ($p = 0.4151$) (Fig. 1 g-k).

In 12-month-old *Col18a1*$^{-/-}$ mice, the occurrence of erythrocyte thrombi was not further increased or even decreased compared to that in 5-month-old *Col18a1*$^{-/-}$ mice, and at this age, there was no difference in the level of erythrocyte accumulation between genotypes (Fig. 1 b-k). The interaction between the age and genotype was significant for the number of capillary erythrocyte thrombi in CA1 ($p = 0.0054$), CC ($p = 0.0119$), and thalamus ($p = 0.0456$) and for arteriolar erythrocyte thrombi in BG ($p = 0.0486$).

In *Col18a1*$^{-/-}$ mice, we found no significant differences in PVS (Fig. 1 a, right) across all studied regions and ages in 5-month-old and 12-month-old animals (**Suppl. Fig. S1 a-d**). Both genotypes had no microbleeds in the mentioned brain regions and age groups.

Knockout of Col18a1 increases BBB leakage

Next, we examined the effects of *Col18a1* deficiency on BBB breakdown, which was assessed by measuring the leakage of immunoglobulin G (IgG) and quantitatively determined as the percentage of small vessel area labeled by *Solanum tuberosum* lectin conjugated to fluorescein isothiocyanate (STL-FITC) in which IgG was detected. Data were collected from six brain regions, namely, the RSC, dorsal striatum (DS), CA1, BG, thalamus and medial prefrontal cortex (mPFC). In young *Col18a1*$^{-/-}$ animals, we revealed that BBB breakdown was significantly increased to ≈ 20 % in the DS and to ≈ 25 % in the thalamus (Mann-Whitney test: $p = 0.0484$ for both regions), with no significant changes in other brain regions (Fig. 2 a & c). The Mann-Whitney test was used here for statistical analysis instead of two-way RM ANOVA due to prominent differences in variability between regions and genotypes and non-Gaussian distribution of values. In 12-month-old mice, we selected two brain regions, CA1 and RSC, for analysis of BBB leakage, as these are highly relevant to CSVD and other age-related disorders, such as Alzheimer's disease (AD) [36–38], and many behavioral and electrophysiological assays have been established to measure the functional impact of abnormalities in these regions. The IgG leakage was ≈ 60 % higher in the CA1 region and RSC of *Col18a1*$^{-/-}$ mice than in *Col18a1*$^{+/+}$ mice (two-way RM ANOVA, Sidak's multiple comparisons test for CA1 and RSC: $p < 0.0001$) (Fig. 2 b & d). Besides IgG, we confirmed leakage of plasma fibrinogen into the RSC parenchyma in 12-month-old *Col18a1*$^{-/-}$ mice **(Suppl. Fig. S2)**. As expected for wild-type mice [33], there was a low IgG signal (≈ 3 % in 12-month-old *Col18a1*$^{+/+}$ mice; CA1 and RSC) in the brain parenchyma of these animals. As we found prominent differences between genotypes in CA1 and RSC, we focused our next analyses on these regions.

Deficiency in Col18a1 activated endothelial cells and altered the basement membranes and tight junctions

To better understand the potential casuses for the BBB breakdown, we determined the mRNA levels of TJ proteins claudin-5 (*Cldn5),* occludin *(Ocln),* zonula occludens-1 (*Zo1*) and basement membrane components (*Col3a1, Col4a1, Col8a1, Lama5, Nid1*), vascular cell adhesion molecule 1 (*Vcam1),* intercellular adhesion molecule 1 (*Icam1*), lysyl oxidase-like 2 (*Loxl2)* and P-glycoprotein (*Pgp*) in hippocampal homogenates [38] in 12-month-old mice. In *Col18a1*$^{-/-}$ mice, *Col3a1, Col4a1, Col8a1, Nid1, Vcam1 and Loxl2* mRNA expression levels were significantly higher than those in controls (*t*-test with Welch's correction for *Col3a1:* $p = 0.0180$; *Col4a1:* $p = 0.0112$; *Col8a1:* $p = 0.0119$; *Nid1:* $p = 0.0083$; *Vcam1:* $p = 0.0459$; *Loxl2:* $p = 0.0018$), while the expression levels of *Ocln and Zo1* were reduced ($p = 0.0004$ and $p = 0.0082$, respectively), suggesting that endothelial activation and dysfunction could contribute to the BBB leakage in *Col18a1*$^{-/-}$ mice (Fig. 3 a). The protein levels of occludin in the cortex were, however, normal but the protein levels of VCAM-1, ICAM-1 and glucose transporter 1 (GLUT1) were confirmed to be upregulated (*t*-test with Welch's correction $p = 0.0253$ and $p = 0.0025$ and $p = 0.0091$, respectively), which supports an evidence for activation of endothelial cells (Fig. 3 **b & c; Suppl. Fig. S3**).

No changes in the density of pericytes and no vascular accumulation of β-amyloid in Col18a1$^{-/-}$ *mice*

Pericytes play a crucial role in responding to injury and producing pro-inflammatory cytokines [39] in various diseases, including ischemic strokes and AD, as a vital component of the neurovascular unit. In this study, we investigated the mRNA level of platelet-derived growth factor receptor beta (*Pdgfrb*) as a marker for pericytes in the hippocampus of *Col18a1*$^{-/-}$ mice compared to control mice. We found that *Pdgfrb* was overexpressed in *Col18a1*$^{-/-}$ mice (*t*-test with Welch's correction $p = 0.0344$) (**Suppl. Fig. S4 a**). Western blot analysis showed that *Col18a1*$^{-/-}$ mice had elevated levels of PDGFRβ (*t*-test with Welch's correction $p = 0.0288$), further suggesting the upregulation of this receptor expression (**Suppl. Fig. S4 b & c**). However, we did not observe any changes in the expression of pericyte surface marker *Cd13* (**Suppl. Fig. S4 a**), suggesting no gross changes in the number of pericytes. In line with these findings, no difference between *Col18a1*$^{-/-}$ and *Col18a1*$^{+/+}$ mice was detected by immunohistochemical analysis of PDGFRβ expression levels in αSMA-immunopositive arterioles and αSMA-immunonegative capillaries (**Suppl. Fig. S4 d**). Quantification of the pericyte density also did not reveal any significant difference between the genotypes (**Suppl. Fig. S4 e**). Furthermore, chondroitin sulfate proteoglycan 4 (*Cspg4),* expressed in oligodendrocyte progenitor cells (OPC) and pericytes, remained unchanged (**Suppl. Fig. S4a**). Although we found decreased mRNA levels of alpha-smooth muscle

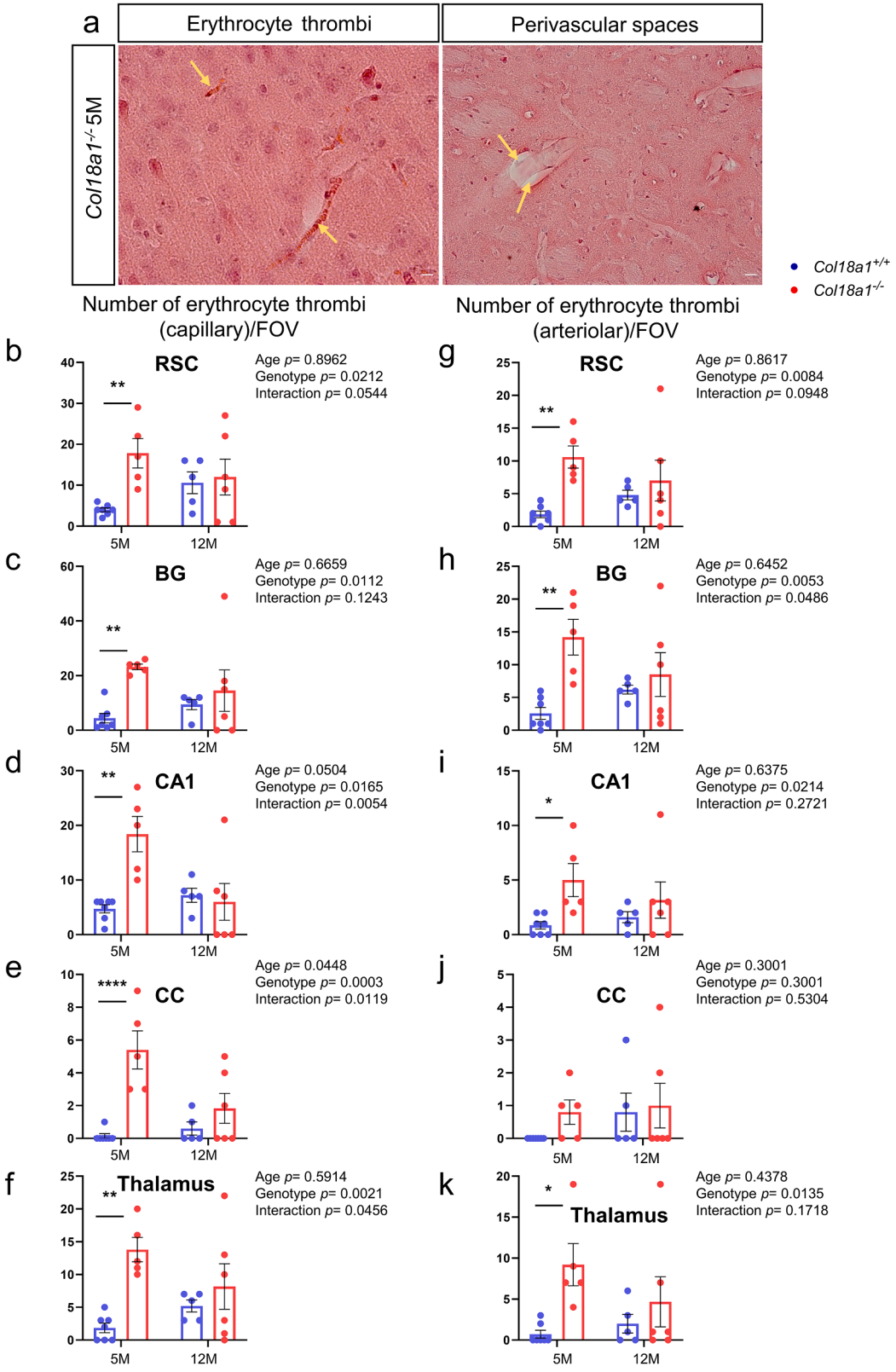

Fig. 1. Erythrocyte thrombi and enlarged perivascular spaces in the brains of *Col18a1*$^{-/-}$ mice. (**a**) Hematoxylin-eosin staining with representative examples of erythrocyte thrombi (arrows) and perivascular spaces (arrows) in 5-month-old *Col18a1*$^{-/-}$ mice. **(b-k),** The mean number (± SEM) of capillary and arteriolar thrombi per animal across five brain regions (RSC, BG, CA1, CC and thalamus) in 5-month-old and 12-month-old animals. Each dot represents one animal. * $p < 0.05$, ** $p < 0.01$, and **** $p < 0.0001$ represent significant differences between *Col18a1*$^{+/+}$ (5-month-old animals: $N = 7$; 12-month-old animals: $N = 5$) and *Col18a1*$^{-/-}$ mice (5-month-old animals: $N = 5$; 12-month-old animals: $N = 6$) using two-way ANOVA and Sidak's multiple comparisons test. BG, basal ganglia; CA1, CA1 region of the hippocampus; CC, corpus callosum; FOV, field of view; M, months; RSC, retrosplenial cortex. Scale bar = 50 μm.

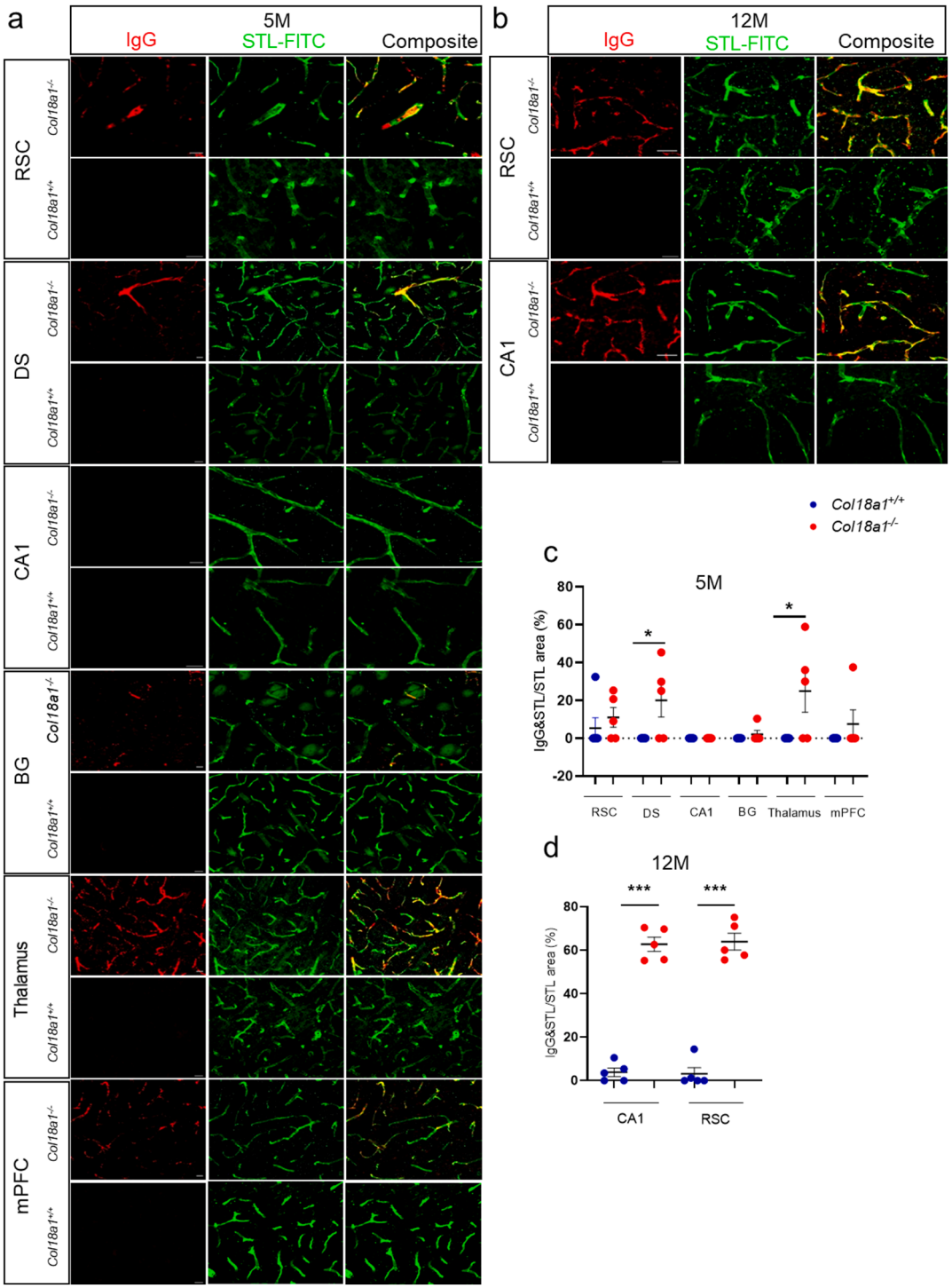

Fig. 2. Knockout of *Col18a1* induces BBB breakdown (a & b). Representative 20x and 40x images of vessels from *Col18a1*$^{-/-}$ and control mice stained with STL-FITC (green) to visualize blood vessels and IgG (red) as a marker of BBB disruption in 5-month-old (5 M) and 12-month-old (12 M) mice, respectively. The percentage of STL-FITC area that colocalized with IgG (yellow in the composite image in **(a & c)**) was calculated in 6 brain regions (RSC, DS, CA1, BG, thalamus and mPFC) of 5-month-old animals and 2 brain regions (CA1, RSC) of 12-month-old animals **(b & d)**. The graphs show mean number ± SEM. Each dot represents one animal. * $p < 0.05$ and *** $p < 0.001$ represent significant differences between *Col18a1*$^{+/+}$ (5-month-old animals: $N = 6$; 12-month-old animals: $N = 5$) and *Col18a1*$^{-/-}$ mice (5-month-old animals: $N = 5$; 12-month-old animals: $N = 5$) using the Mann-Whitney test for young animals and two-way RM ANOVA and Sidak's multiple comparisons test for old animals. AT, anterior thalamus; BBB, blood-brain barrier; BG, basal ganglia; CA1, CA1 region of the hippocampus; DS, dorsal striatum; GAPDH, glyceraldehyde 3-phosphate dehydrogenase; IgG, immunoglobulin G (BBB breakdown detection); M, months; mPFC, medial prefrontal cortex; RSC, retrosplenial cortex; STL-FITC, *Solanum tuberosum lectin* fluorescein isothiocyanate (endothelial marker). Scale bars = 20 μm.

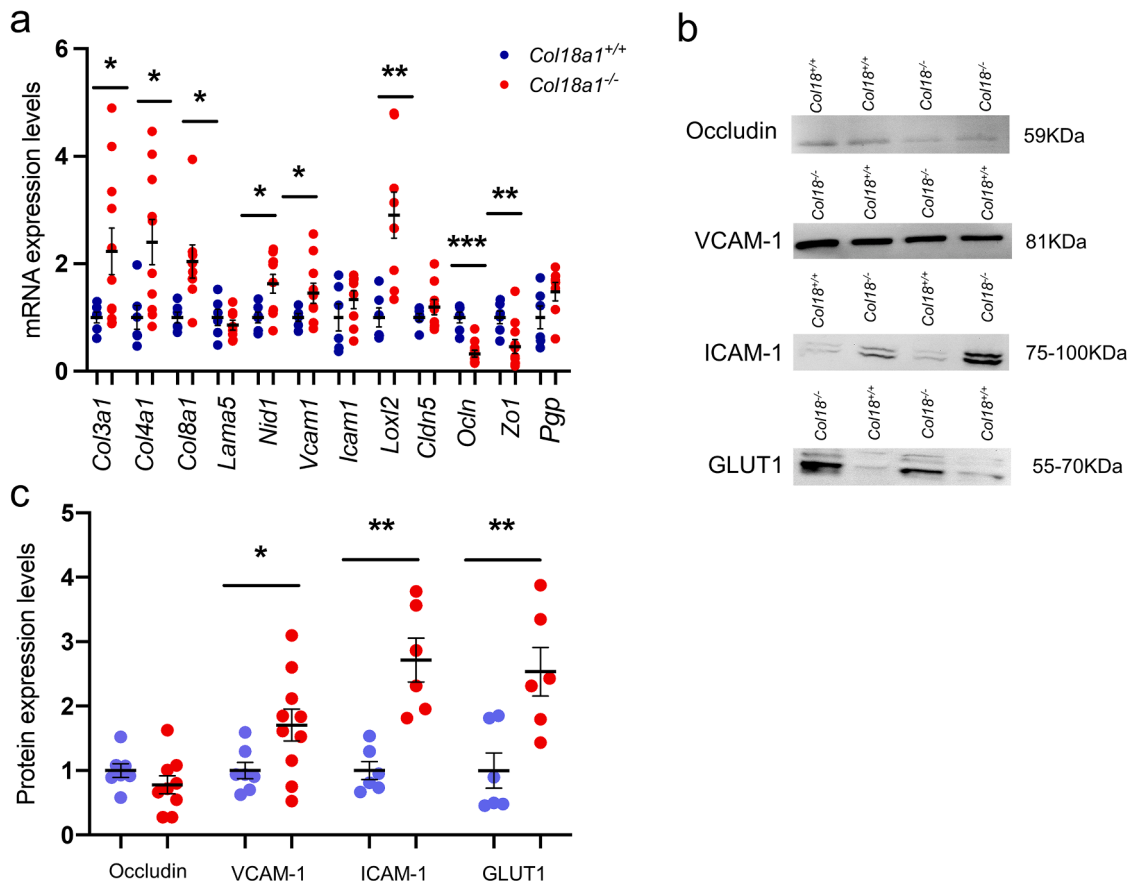

Fig. 3. Knockout of *Col18a1* activates endothelial cells and alters the expression of basement membrane proteins. (a) The expression of genes involved in the organization of the basement membrane in the hippocampal region of 12-month-old mice was investigated using RT-qPCR and normalized to individual GAPDH values. Graphs show the mean ± SEM and individual values; *t*-test with Welch's correction: * $p < 0.05$, ** $p < 0.01$, and *** $p < 0.001$. **(b & c)** Representative western blots for the expression of occludin, VCAM-1, ICAM-1 and GLUT1 in the cortex region of 12-month-old mice. * $p < 0.05$ represent significant differences between *Col18a1*$^{+/+}$ ($N = 6$) and *Col18a1*$^{-/-}$ mice ($N = 11$).

actin (*Acta2*) (*t*-test with Welch's correction $p = 0.0399$) in *Col18a1*$^{-/-}$ mice **(Suppl. Fig. S4a)**, no changes were revealed by immunohistochemical evaluation of vascular expression of this protein in these mice (**Suppl. Fig. S4 d & e**). Thus, no consistent changes were detected in pericytes and smooth muscle cells in *Col18a1*$^{-/-}$ mice using different approaches for expression analysis.

Immunolabelling of mouse β-amyloid [40] revealed a diffuse pattern of expression with accumulation in somata of some cells and no accumulations in vessels in both *Col18a1*$^{+/+}$ and *Col18a1*$^{-/-}$ mice (**Suppl. Fig. S5**), suggesting that the deficiency in *Col18a1* does not result in cerebral amyloid angiopathy (CAA) at least in the studied ages.

Microglial activation and recruitment to cerebral small blood vessels in Col18a1$^{-/-}$ *mice*

Using IHC staining with an antibody against the ionized calcium-binding adaptor molecule 1 (Iba1) and STL-FITC, we visualized microglia/perivascular macrophages and blood vessels within the CA1 region, observing some microglia/perivascular macrophages in close association with small vessels (Fig. 4 a i & ii) [41]. To quantify the colocalization of vessels and vessel-associated microglia (VAM)/perivascular macrophages, we employed color thresholding and binary analysis (Fig. 4 a iii). This colocalization significantly increased by 15 % in *Col18a1*$^{-/-}$ mice compared to *Col18a1*$^{+/+}$ mice (*t*-test with Welch's correction $p = 0.0091$; Fig. 4 c), suggesting that microglia/macrophages were recruited to cerebral vessels in *Col18a1*$^{-/-}$ mice.

To understand the mechanism behind microglial cell migration, we investigated the expression of a chemokine that might be involved in the recruitment of microglia. The mRNA level of chemokine (C—C motif) ligand 2 (*Ccl2)* which is secreted from endothelial cells, smooth muscle cells, astrocytes and fibroblasts was elevated in *Col18a1*$^{-/-}$ mice compared to *Col18a1*$^{+/+}$ mice (*t*-test with Welch's correction $p = 0.0077$, Fig. 4 d).

It has been reported that BBB breakdown is associated with increased glial activation and release of neuroinflammatory factors. Therefore, the alterations in microglia in 12-month-old mice were investigated using Iba1 immunohistochemistry. Although Iba1 expression per se does not allow to reliably differentiate between resting and activated microglia [42], 2D and 3D morphological analyses of Iba1-stained microglia, showcased in Fig. 4b, effectively discriminated between resting and activated states. Analysis of microglial morphology in the RSC and CA1 region revealed that Iba1-labeled microglia appeared to display a more spherical morphology in *Col18a1*$^{-/-}$ mice compared to the ramified appearance in control mice (Fig. 4 b & e-f). At 12 months, *Col18a1*$^{-/-}$ mice had a larger microglial somatic area by 20 % in CA1 (two-way RM ANOVA, Sidak's multiple comparisons test; $p = 0.0464$) and by 37 % in the RSC (two-way RM ANOVA, Sidak's multiple comparisons test; $p = 0.0014$) than in the corresponding regions of *Col18a1*$^{+/+}$ mice (Fig. 4 e). The average branch lengths of microglial processes were significantly reduced in the CA1 region compared to controls (two-way RM ANOVA, Sidak's multiple comparisons test; $p = 0.0051$; Fig. 4 f). Additionally, in the RSC of *Col18a1*$^{-/-}$ mice, we revealed an increase in the density of microglial cells (two-way RM ANOVA, Sidak's multiple comparisons test; $p = 0.0168$, Fig. 4 g). In 5-month-old mice, we found, however, that

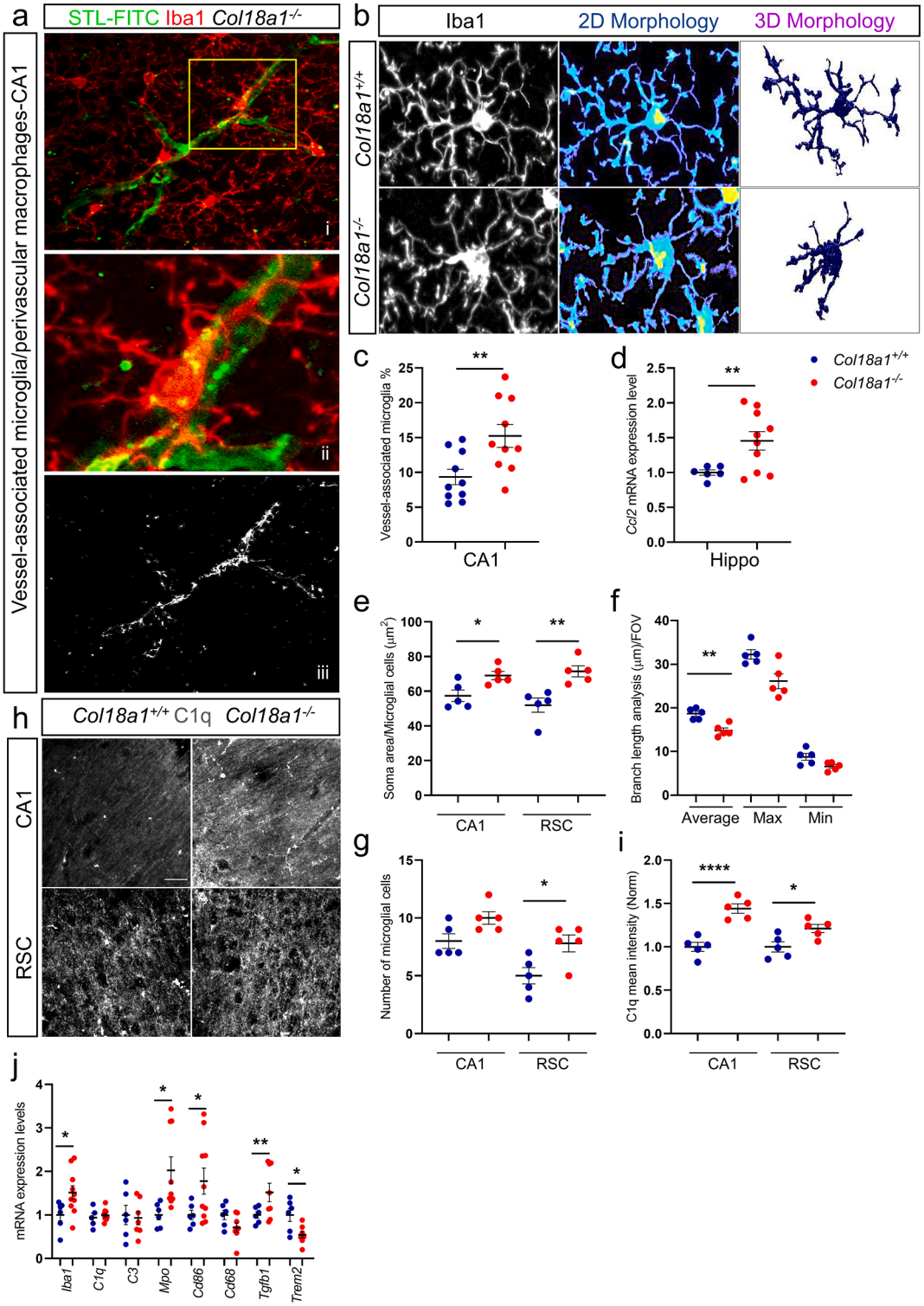

Fig. 4. Microglial activation and microglia/perivascular macrophage recruitment to cerebral small blood vessels in *Col18a1*$^{-/-}$ mice. (a) Representative 40x image of the CA1 area *in Col18a1*$^{-/-}$ mice showing microglial/perivascular macrophages (Iba1, red) associated with blood vessels (STL-FITC, green). Middle: magnified part of the image **(ii)** outlined on the **(i)** in yellow. **(iii)**: colocalization of Iba1 and STL-FITC. **(c)**, Increased colocalization in *Col18a1*$^{-/-}$ mice. **(d)** Overexpression of *Ccl2*, a gene involved in microglial recruitment. Data are presented as the mean ± SEM. Each dot represents one FOV in **(c)** and one animal in **(d)**. * $p < 0.05$, ** $p < 0.01$, and **** $p < 0.0001$, represent significant differences between *Col18a1*$^{+/+}$ ($N = 5$) and *Col18a1*$^{-/-}$ mice ($N = 5$) in 12-month-old animals in **(c)** and *Col18a1*$^{+/+}$ ($N = 6$) and *Col18a1*$^{-/-}$ mice ($N = 11$) **(d)** using the *t*-test with Welch's correction. **(b)** Activation of microglia was confirmed by immunostaining in the RSC and hippocampal CA1 area, which revealed an increase in the soma area **(e)** and a decrease in the branch length **(f),** which correlated with the increasing number of microglial cells **(g)** in *Col18a1*$^{-/-}$ mice. **(h & i)** Representative images showing the upregulation of C1q immunostaining in the CA1 and RSC of *Col18a1*$^{-/-}$ mice. **(j)** Representative expression of genes involved in microglial activation and subtypes differentiation using RT-qPCR and normalized to individual GAPDH values. CA1, CA1 region of the hippocampus; *Ccl2*, (C—C motif) ligand 2; FOV, field of view; GAPDH, glyceraldehyde 3-phosphate dehydrogenase; Hippo – hippocampus; Iba1, ionized calcium-binding adapter molecule 1; IgG, immunoglobulin G; RSC, retrosplenial cortex; STL-FITC, *Solanum tuberosum lectin* fluorescein isothiocyanate (endothelial marker); VAM, vessel-associated microglia/perivascular macrophages. Scale bars = 20 μm.

the expression of microglial IBA1 in CA1 and RSC was normal compared to control mice (**Suppl. Fig. S6 a**). Our findings thus demonstrate that there is a correlation between age-dependent BBB breakdown and alterations in microglial cell morphology and density in these brain regions.

As complement component 1 (C1q) may promote synaptic phagocytosis by microglia, we examined the association between C1q and *Col18a1* deficiency. Our data revealed that C1q was upregulated by 44 % in the neuropil of the CA1 region and by 21 % in the RSC (two-way RM ANOVA, Sidak's multiple comparisons test; $p < 0.0001$ and $p = 0.0245$, respectively; Fig. 4 h & i), although the overall hippocampal mRNA expression of *C1q* remained unchanged (Fig. 4 j). Similarly, the mRNA level of *C3* and *Cd47* remained unchanged (Fig. 4 j). These results suggest that *Col18a1* deficiency may be associated with increased levels of C1q in specific regions of the brain, which may affect synaptic pruning by microglia.

Our gene expression evaluation strongly supported these observations, suggesting a contribution of transcriptional regulations (Fig. 4 j). We detected significant increases in the expression of genes characteristic for activated microglial cells, including *Iba1* (*t*-test with Welch's

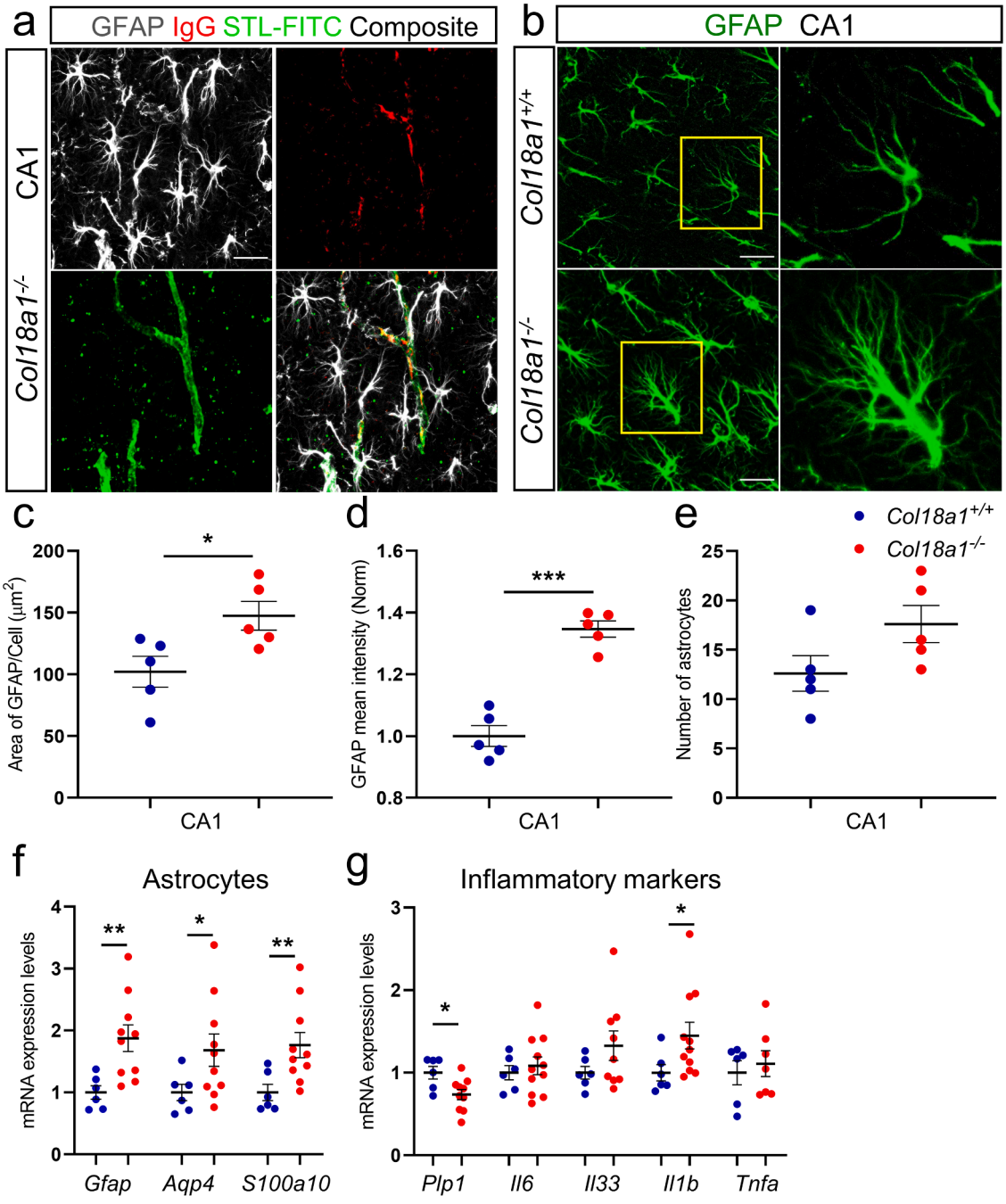

Fig. 5. Activation of astrocytes and expression of inflammatory markers in 12-month-old *Col18a1*$^{-/-}$ mice. (a) Representative image of reactive astrocytes in association with damaged vessels in the hippocampal region of *Col18a1*$^{-/-}$. **(b)** Representative fluorescent images showing GFAP-labeled astrocytes (green). **(c & d)** An increase in GFAP^{+} cell area and mean intensity was observed, while the density of GFAP^{+} cells remained unchanged **(e)** in the hippocampal CA1 region of *Col18a1*$^{-/-}$ mice. Data are presented as the mean ± SEM, while * $p < 0.05$, ** $p < 0.01$ and *** $p < 0.001$ and represent significant differences between *Col18a1*$^{+/+}$ ($N = 5$) and *Col18a1*$^{-/-}$ ($N = 5$) mice using, and *t*-test with Welch's correction. Scale bars = 20 µm. **(f & g)** Expression of genes involved in astrocytes **(f)** and **(g)** inflammation and related molecules were investigated using RT-qPCR and normalized to individual GAPDH values.

correction here and below $p = 0.027$), myeloperoxidase *(Mpo)* ($p = 0.0114$), *Cd86* ($p = 0.0319$), and transforming growth factor beta 1 (*Tgfb1)* ($p = 0.0487$). In contrast, we observed a significant decrease in triggering receptor expressed on myeloid cells 2 *(Trem2)* ($p = 0.0275$), which controls the switch of microglial transcriptome programming that modulates microglial chemotaxis, phagocytosis, and microglial regulation of synaptic function.

Activation of astrocytes and expression of inflammatory markers in Col18a1$^{-/-}$ mice

Next, we assessed the state of astrocytes by measuring glial fibrillary acidic protein (GFAP) immunofluorescence within the CA1 region as well as by counting the number of astrocytes in 12-month-old mice. An analysis of GFAP$^+$ cell area and mean intensity in *Col18a1*$^{-/-}$ mice revealed significant increases in both parameters (*t*-test with Welch's correction $p = 0.0295$ and $p < 0.0001$, respectively), although no changes in the number of GFAP$^+$ cells were observed (Fig. 5 a-e). Subsequently, in our extended analysis aimed at pinpointing the onset of astrocyte activation, we immunostained 5-month-old mice and observed no signs of activation in astrocytes in the CA1 region (**Suppl. Fig. S6 b)**.

In line with our staining, we detected a significant increase in the expression of *Gfap* (*t*-test with Welch's correction here and below, $p = 0.0030$) (Fig. 5 f). Moreover, expression of other astrocytic genes was upregulated including aquaporin 4 *(Aqp4)* ($p = 0.0366$) and *S100a10* ($p = 0.0072$), which is a marker of the A2 astroglial subtype and plays important roles in intracellular trafficking and cell migration [43]. Immunohistochemically, however, the level and pattern of AQP4 expression were found to be normal in *Col18a1*$^{-/-}$ mice (**Suppl. Fig. S7)**.

As proteolipid protein 1 (PLP1) is one of the main protein components in myelin of the central nervous system (CNS) and myelination defects are characteristic of the disease and reflected by oligodendrocyte damage, we examined the hippocampal mRNA expression level of *Plp1* and found that it was downregulated (*t*-test with Welch's correction $p = 0.0218$) (Fig. 5 g)

Furthermore, the hippocampal mRNA expression of the proinflammatory cytokine *Il1b* which is secreted by microglia, astrocytes, neurons and endothelial cells, was significantly increased (*t*-test with Welch's correction $p = 0.0306$) in *Col18a1*$^{-/-}$ compared to control mice, whereas no changes were seen in the hippocampal levels of other proinflammatory cytokines, *Il6, Tnfa,* and *Il33.* The latter is expressed by neurons in an activity-dependent manner to control microglial activity towards the neural ECM [44](Fig. 5 g). These data point to a specific role for *Il1b* upregulation in the inflammatory response observed in *Col18a1*$^{-/-}$ mice.

Reduced expression of parvalbumin and perineuronal nets in Col18a1$^{-/-}$ mice

Because of microglial activation in *Col18a1*$^{-/-}$ mice and an established interaction between microglia and parvalbumin (PV$^+$) interneurons [45], we studied the effects of *Col18a1* deficiency on the size of PV$^+$ cells and the level of their PV expression as measures reflecting their function. Using PV immunolabeling (Fig. 6 a) and quantitative analysis of 12-month-old mice, we found that the mean intensity of PV$^+$ cells in CA1 and RSC decreased by 25 % and 44 %, respectively (two-way RM ANOVA, Sidak's multiple comparisons test; $p = 0.0128$ and $p < 0.0001$; respectively; Fig. 6 b) in *Col18a1*$^{-/-}$ mice when compared to wild-type controls. Furthermore, the area of PV$^+$ cells was reduced by 22 % in CA1 (two-way RM ANOVA, Sidak's multiple comparisons test $p = 0.0162$; Fig. 6 c).

Additionally, the mean intensity of the proteoglycan Aggrecan (Acan) colocalizing with CA1 PV$^+$ interneurons (Fig. 6 a), a measure of the structural integrity of associated perineuronal nets (PNNs), and the size of Acan$^+$ PV$^+$ cells were reduced in *Col18a1*$^{-/-}$ mice compared to

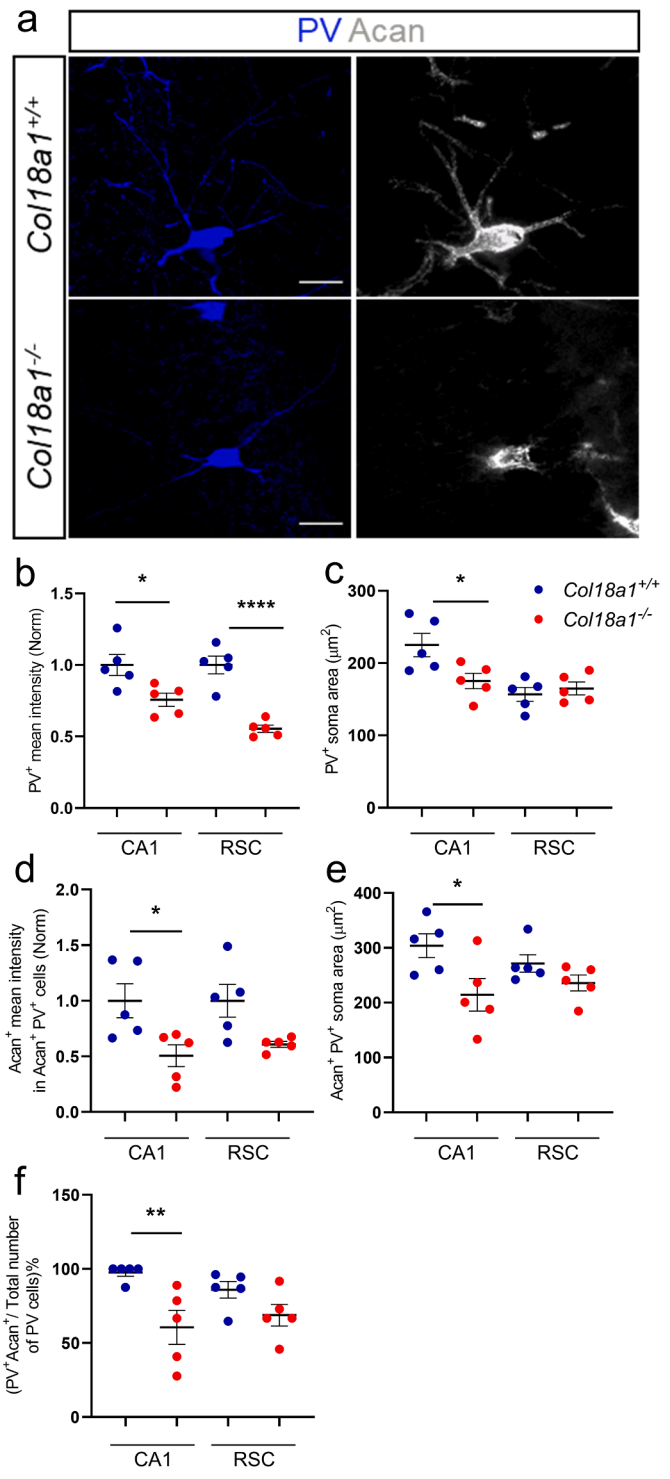

Fig. 6. Reduced expression of parvalbumin and aggrecan of perineuronal nets in *Col18a1*$^{-/-}$ mice. (a) Representative 40x images of morphologically dystrophic PV$^+$ interneurons associated with Acan in *Col18a1*$^{-/-}$ mice. **(b & c),** Quantification of PV$^+$ interneurons associated with *Col18a1*$^{-/-}$ mice revealed significant reductions in the mean PV+ intensity and area in the hippocampal CA1 region. **(d & e)** The mean Acan intensity **(d)** and area **(e)** of Acan$^+$ PV$^+$ cells were significantly reduced in the hippocampal CA1 of *Col18a1*$^{-/-}$ mice. **(f)** The percentage of PV$^+$ cells surrounded by Acan per total number of PV cells significantly decreased in the hippocampal CA1 of *Col18a1*$^{-/-}$ mice.* $p < 0.05$, ** p and < 0.01, RM ANOVA followed by Sidak's multiple comparisons test.

Col18a1$^{+/+}$ mice (two-way RM ANOVA, Sidak's multiple comparisons test; $p = 0.0179$, $p = 0.0182$, respectively; Fig. 6 d & e). However, these measures did not show any changes in the RSC region. Moreover, there was a 37 % decrease in the fraction of Acan^{+}PV^{+} cells per total PV^{+} cell population in the CA1 region of *Col18a1*$^{-/-}$ mice (Fig. 6 f).

Alterations in glutamatergic synapses in Col18a1$^{-/-}$ *mice*

Considering the activation of microglia and astrocytes in *Col18a1*$^{-/-}$ mice, we investigated possible changes in synaptic markers and the associated perisynaptic ECM. The mean fluorescence intensity of the vesicular glutamate transporter 1 (VGLUT1) as excitatory presynaptic marker was decreased in 12-month-old *Col18a1*$^{-/-}$ mice in the neuropil of the CA1 region by 45 % (two-way RM ANOVA, Sidak's multiple comparisons test; $p = 0.0002$) and in the RSC by 37 % (two-way RM ANOVA, Sidak's multiple comparisons test; $p = 0.0014$; Fig. 7 a & b). In contrast, the fluorescence intensity of VGLUT2 (Fig. 7 c & d), which is predominantly expressed in another subset of glutamatergic presynapses, was not different between genotypes (Fig. 7 d). Additionally, the expression of the presynaptic GABAergic marker VGAT was not affected by *Col18a1* deficiency (Fig. 7 e & f). Notably, 5-month-old mice did not exhibit a reduction in the protein level of VGLUT1 (Suppl. Fig. S6 c).

In line with the observed reduction in presynaptic VGLUT1, the expression of the glutamatergic postsynaptic scaffold protein Homer1 was reduced by 27 % in the CA1 region (two-way RM ANOVA, Sidak's multiple comparisons test; $p = 0.0290$; Fig. 7 g & h).

Upregulation of perisynaptic ECM proteoglycan Brevican and downregulation of presynaptic VGLUT1 in Col18a1$^{-/-}$ *mice*

To further investigate changes in excitatory synapses and the associated perisynaptic ECM, we performed double VGLUT1/Brevican (Bcan) immunolabeling (Fig. 8 a & b), confocal imaging and applied a recently developed script for image analysis of synaptic puncta and perisynaptic Bcan expression [44]. In agreement with measurements of the VGLUT1^{+} mean intensity per ROI (Fig. 7 b), analysis of single VGLUT1^{+} puncta intensity revealed a 51 % decrease in CA1 (two-way RM ANOVA, Sidak's multiple comparisons test; $p < 0.0001$) and 32 % in RSC ($p = 0.001$) (Fig. 8 c); however, the number of VGLUT1^{+} puncta in the neuropil remained unchanged in *Col18a1*$^{-/-}$ mice (Fig. 8 d). The total expression of Bcan was upregulated: the mean intensity per ROI was increased by 58 % in CA1 (two-way RM ANOVA, Sidak's multiple comparisons test; $p = 0.0118$) and by 75 % in the RSC (two-way RM ANOVA; Sidak's multiple comparisons test $p = 0.0017$) (Fig. 8 e). Also, the perisynaptic expression of Bcan in the area around presynaptic puncta was elevated by 28 % in CA1 (two-way RM ANOVA, Sidak's multiple comparisons test; $p = 0.0357$) and by 33 % in the RSC (two-way RM ANOVA, Sidak's multiple comparisons test; $p = 0.0119$) (Fig. 8 f). Interestingly, we found no changes in Bcan expression in 5-month-old *Col18a1*$^{-/-}$ (**Suppl. Fig. S6 d)**. Thus, an age-dependent pattern of Bcan dysregulation goes hand-in-hand with vascular and inflammatory alterations.

Next, we analyzed the total Bcan expression level in the cortical homogenate. For the detection of full-length 145 KDa and proteolytically cleaved Bcan, we used an antibody that detects all isoforms including the major 80 kDa fragment (Fig. 8 g & h). Our results indicated that the amount of full-length Bcan in *Col18a1*$^{-/-}$ mice was significantly higher than in *Col18a1*$^{+/+}$ mice (*t*-test with Welch's correction $p = 0.0093$), while the amount of cleaved Bcan remained unchanged (*t*-test with Welch's correction $p = 0.1073$) although showed a similar tendency as the full-length Bcan. Consistency, the ratio of the cleaved fragment to full-length Bcan also remained unchanged (*t*-test with Welch's correction $p = 0.8144$), favoring a view that the protein synthesis rather than proteolysis of Bcan is predominantly altered in *Col18a1*$^{-/-}$ mice.

Evaluation of gene expression of chondroitin sulfate proteoglycans, enzymes regulating their proteolysis and TGFβ1/Smad3 signaling in Col18a1$^{-/-}$ *mice*

Further, we extended our expression analysis of ECM-related genes to gain insight into the mechanisms underlying the dysregulation of neural ECM in *Col18a1*$^{-/-}$ mice. We observed a significant mRNA overexpression of *Acan* (*t*-test with Welch's correction here and below, $p = 0.0214$) along with downregulation of neurocan (*Ncan*) and *Bcan* ($p = 0.0231$ and $p = 0.0168$, respectively) (Fig. 9 a). Moreover, the expression of the link protein hyaluronan and proteoglycan link protein 4 (*Hapln4)* and of the CSPG cross-linking glycoprotein tenascin-R (*Tnr)* was significantly increased ($p = 0.0081$ and $p = 0.0017$, respectively), while the expression of *Hapln3* was decreased ($p = 0.0297$), and there was no change in the expression of *Hapln2* ($p = 0.1276$) (Fig. 9 a). Furthermore, the expression of tissue metalloproteinases inhibitor 3 *(Timp3)* ($p = 0.0309$), metalloproteinase with thrombospondin type 1 motif, 4 (*Adamts4)* ($p = 0.0175$), matrix metallopeptidase 2 (*Mmp2)* ($p = 0.0463$) and cathepsin S *(Ctss)* ($p = 0.0235$) was significantly increased, while the expression of matrix metallopeptidase 9 (*MMP9)* ($p = 0.0086$*)* was decreased. There were no changes observed in the expression of *Timp1, Timp2, Timp4* and metalloproteinase with thrombospondin type 1 motif, 5 (*Adamts5*) (Fig. 9 b). In summary, our findings demonstrate a complex pattern of changes in the gene expression of ECM proteins, which could be contributing to the observed alterations in perineuronal and perisynaptic ECM stability and proteolysis.

As TIMP-3 plays a crucial role in regulating multiple proteinases, including ADAMTS-4 and 5, which cleave CSPGs, we performed Western blot analysis to determine the protein level of TIMP-3 in *Col18a1*$^{-/-}$ mice. Our analysis revealed a significant upregulation of this protease inhibitor (*t*-test with Welch's correction, $p = 0.0302$) (Fig. 9 c & d), while the protein level of ADAMTS-4 remained unchanged in *Col18a1*$^{-/-}$ mice (*t*-test with Welch's correction, $p = 0.2342$) (Fig. 9 c & d).

To understand the mechanism underlying the increase in ECM proteoglycans and TIMP-3, we examined the signaling pathway mediated by TGF-ß1. Previous research has linked elevated TGF-ß1 signaling to various vascular diseases in humans such as CSVD, hereditary hemorrhagic telangiectasia, Loeys-Dietz syndrome, and pulmonary arterial hypertension [46,47]. Therefore, increased TGF-ß signaling is a strong candidate that may explain matrix accumulation [48,49].

Consistently with our qPCR finding (Fig. 4 j), we observed an upregulation of TGF-ß1 protein level in *Col18a1*$^{-/-}$ mice (*t*-test with Welch's correction, $p = 0.0220$) (Fig. 9 c & d). The TGF-ß/Smad3 pathway has previously been demonstrated to induce ECM production. As Smad3 is the key player in this cascade, we have confirmed a higher phosphorylation level for this protein, i.e. more activated SMAD3, in the *Col18a1*$^{-/-}$ mice (*t*-test with Welch's correction for pSmad3/Smad3 ratio, $p = 0.0422$). Therefore, based on our results, we suggest that TGF-ß1-mediated upregulation of TIMP-3 and ECM proteins is at least partially driven by the canonical Smad3 pathway (Fig. 9 e).

Collagen XVIII expression in small cerebral vessels of hypertensive patients and controls

We also intended to validate the role of COL18 in human autopsy tissue. We decided to investigate COL18 expression in patients with cerebral hypertensive arteriopathy (**Suppl. Table S1**), and this decision was based on our experimental findings particularly mirroring sporadic risk-factor related CSVD in humans, but not amyloid-related CSVD/CAA (**Suppl. Fig. S5**). First, we qualitatively evaluated the distribution of COL18 in control patients without cerebral hypertensive arteriopathy. Here, COL18 was mainly expressed in blood vessels, comprising capillaries, arteries and veins (Fig. 10 a, b), with some diffuse staining in the neuropil and sometimes lipofuscin-like granules in the perikarya. The staining appeared to be located both in endothelial cells and in the basement membranes (Fig. 10 c, d), usually with a discontinuous and

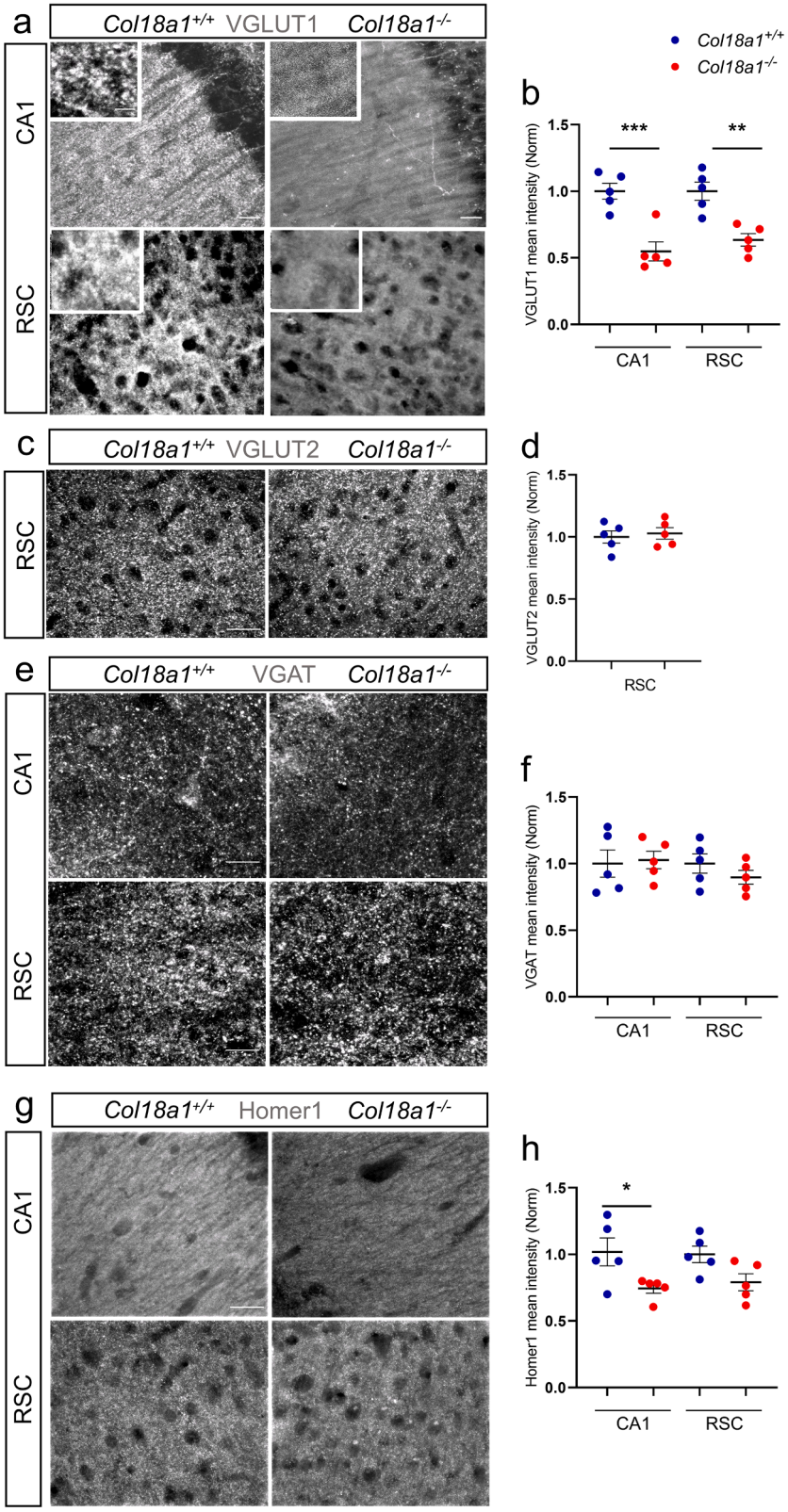

Fig. 7. Alterations in glutamatergic synapses in *Col18a1*$^{-/-}$ mice. (a, c, e & g) Representative 63x and 40x confocal images of VGLUT1 (63x), VGLUT2 (40x), VGAT (40x) and Homer1 (40x) immunostaining in the CA1 and RSC of 12-month-old *Col18a1*$^{-/-}$ and *Col18a1*$^{+/+}$ mice. There was a significant reduction in the fluorescent intensity of VGLUT1 **(b)** and Homer1 **(h)** puncta in *Col18a1*$^{-/-}$ mice in the CA1 and RSC regions, but there was no difference between the genotypes in VGLUT2 expression in the RSC region **(d)** and VGAT in the CA1 and RSC regions **(f)**. Graphs show the mean ± SEM and individual values, while * $p < 0.05$, ** $p < 0.01$, and *** $p < 0.001$ represent significant differences between *Col18a1*$^{+/+}$ ($N = 5$) and *Col18a1*$^{-/-}$ ($N = 5$) mice using two-way RM ANOVA and Sidak's multiple comparisons test. CA1, CA1 region of the hippocampus; Homer 1, homer protein homolog 1; RSC, retrosplenial cortex; VGAT, vesicular GABA transporter; VGLUT1, vesicular glutamate transporter 1; VGLUT2, vesicular glutamate transporter 2. Scale bars = 20 μm.

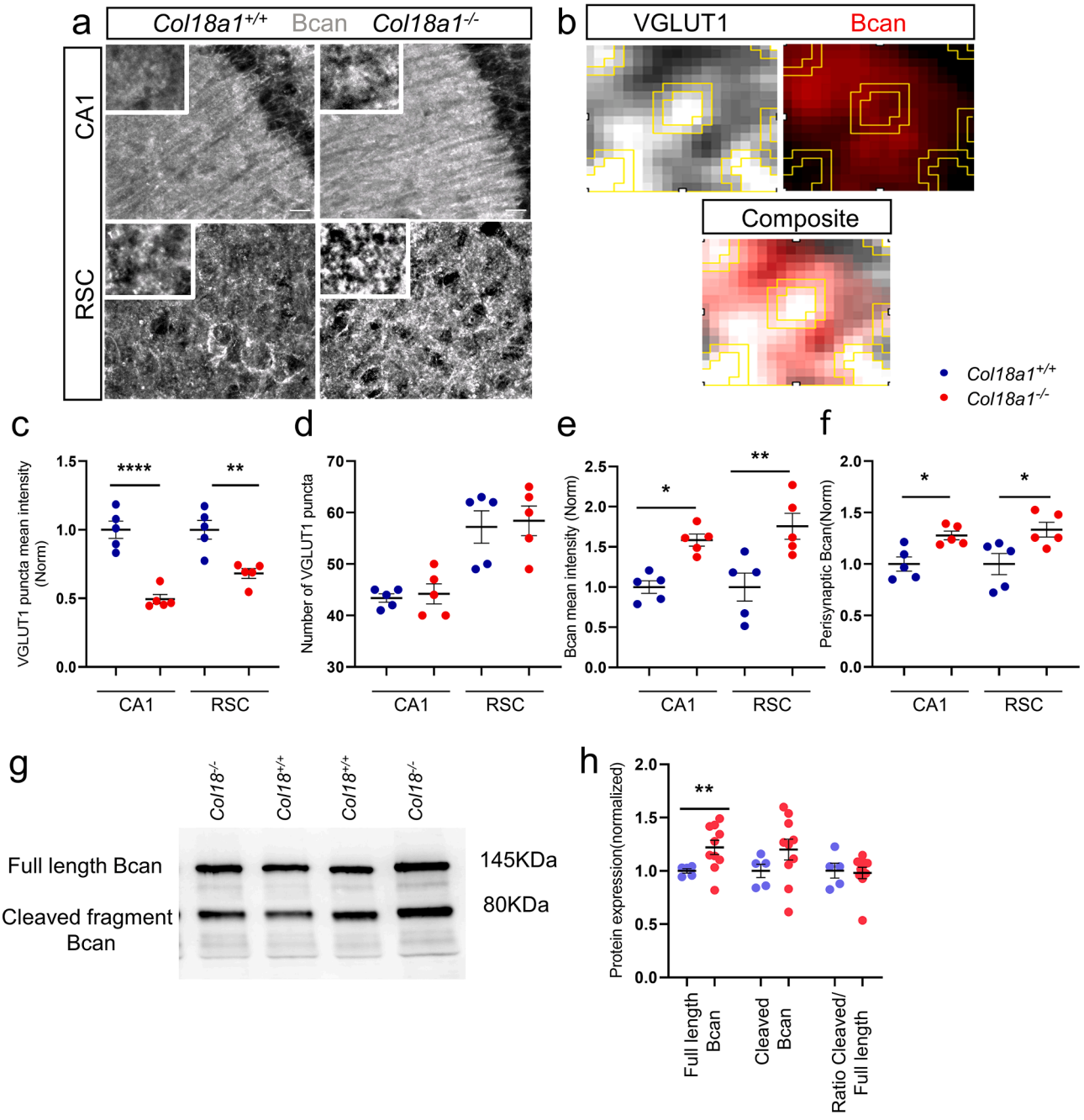

Fig. 8. Upregulation of perisynaptic proteoglycan Bcan and downregulation of presynaptic VGLUT1 in *Col18a1*$^{-/-}$ mice. (a) Representative 63x images of Bcan expression in the CA1 and RSC regions. **(b)** Magnified image of single presynaptic puncta and surrounding ECM to count excitatory synapses and measure the perisynaptic ECM associated with them. **(c & d)** Quantification of VGLUT1^{+} puncta within the CA1 and RSC regions of *Col18a1*$^{-/-}$ mice revealed a significant reduction in the intensity of VGLUT1^{+} puncta **(c)**; however, there were no changes in the number of VGLUT1^{+} puncta **(d)** in the neuropil of *Col18a1*$^{-/-}$ mice. **(e)** The mean intensity of Bcan was significantly increased in the CA1 and RSC of *Col18a1*$^{-/-}$ mice compared to wild-type animals. **(f)** The mean intensity of perisynaptic Bcan was significantly increased in the CA1 and RSC regions of *Col18a1*$^{-/-}$ mice. Graphs show the mean ± SEM and individual values, while * $p < 0.05$, ** $p < 0.01$ and **** $p < 0.0001$ represent significant differences between *Col18a1*$^{+/+}$ mice ($N = 5$) and *Col18a1*$^{-/-}$ ($N = 5$) mice using two-way RM ANOVA and Sidak's multiple comparisons post hoc test. **(g & h)** shows that there is an upregulation in the level of full-length Bcan protein in the cortex of 12-month-old mice, but not the cleaved fragment protein and the ratio level of cleaved fragment/full length. Bar graphs show the mean ± SEM values, while ** $p < 0.01$ represent a significant difference between *Col18a1*$^{+/+}$ ($N = 5$) and *Col18a1*$^{-/-}$ ($N = 10$) mice using a *t*-test with Welch's correction test.

patchy appearance. Some pericyte-like nuclei were also apparent, on occasion, on arterioles (Fig. 10 c), and overall, the most intense staining was identified in larger arterioles and arteries with clear-cut staining in both endothelium and through the smooth muscle cell layer (Fig. 10 d). This was evident for both superficial pial penetrating arteries (Fig. 10 e), and deep-intra-parenchymal vessels. External glia limitans was clearly stained under the pia-mater, and so was the internal glia limitans, with more evident staining in vessels exhibiting uneven staining of the tunica media (Fig. 10 e, f). On occasion, astrocyte-like cytoskeletal profiles could be identified, without any accompanying evident morphological changes, and sometimes the staining was evident only in astrocyte-like nuclei (Fig. 10 g). Regardless of the hypertensive / non-hypertensive state, a particular staining pattern emerged when analyzing the hippocampus, where in the temporal horns of the lateral ventricles we

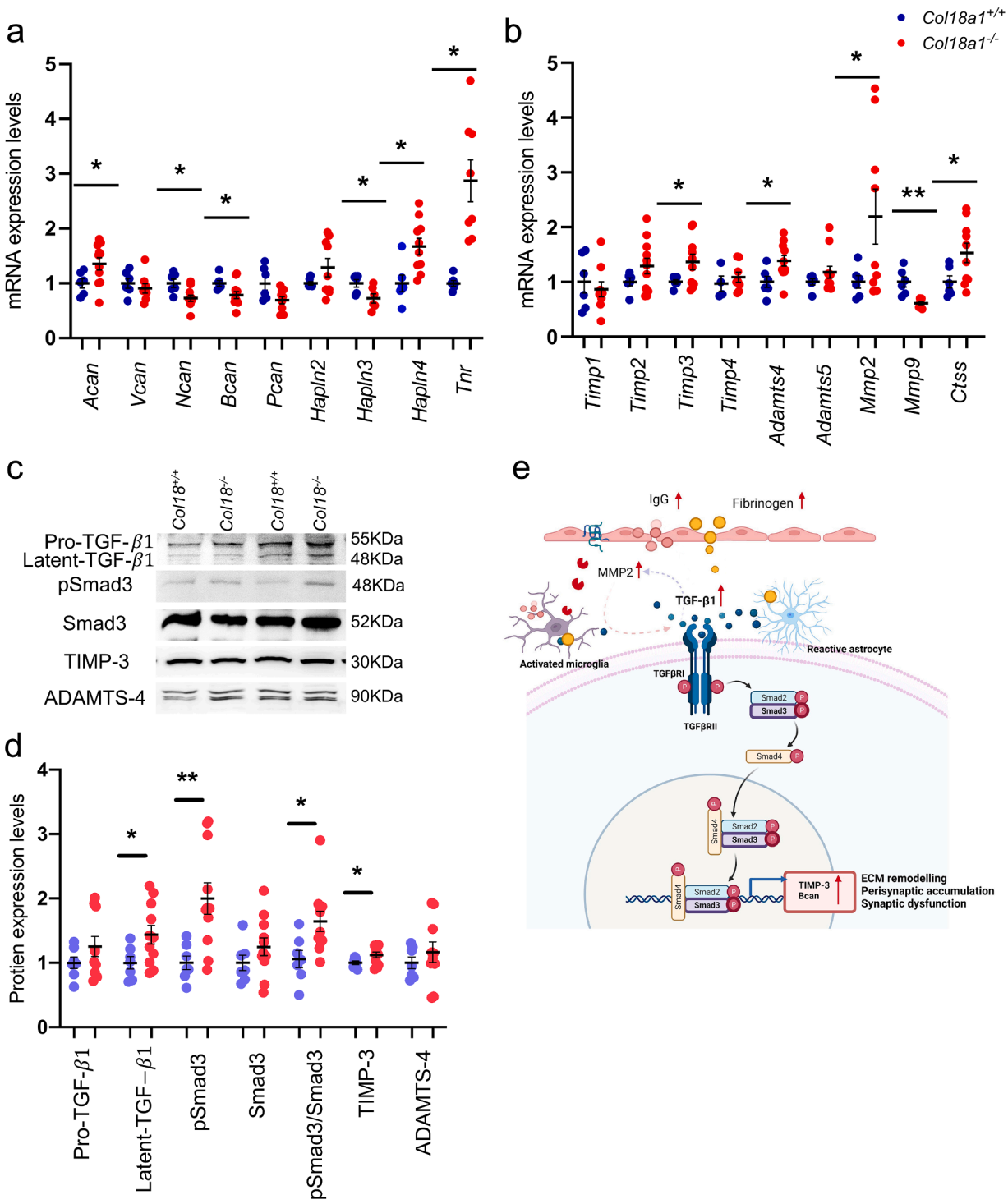

Fig. 9. Evaluation of ECM genes expression and proteins regulating ECM proteolysis and TGF-ß1/Smad3 cascade in *Col18a1*$^{-/-}$ mice. (a) Hippocampal expression of major genes encoding the PNN CSPGs (*Acan, Vcan, Ncan, Bcan and Pcan*), link proteins (*Hapln2, Hapln3, Hapln4*) and *Tnr*. **(b)** Hippocampal expression of genes encoding the tissue metalloprotease inhibitors *Timp1, Timp2, Timp3* and *Timp4* and genes encoding major metalloproteases degrading the neural ECM proteins *Adamts4, Adamts5, Mmp2, Mmp9*, and *Ctss*. **(c & d)** Demonstrated cortical western blot analysis of TGF-ß1, pSmad3/Smad3, TIMP-3 and ADAMTS-4 in the cortex region of 12-month-old mice. Graphs show the mean ± SEM and individual values, while * $p < 0.05$ and ** $p < 0.01$ represent significant differences between *Col18a1*$^{+/+}$ ($N = 6$) and *Col18a1*$^{-/-}$ ($N = 11$) mice using the *t*-test with Welch's correction. **(e)** Due to deficiency in COL18, the BBB breaks down, fibrinogen and albumin are extravasated, and microglia and astrocytes become activated. Activated microglia and reactive astrocytes secrete TGF-ß1 and MMP2. Meanwhile, TGF-ß1 ligand binds to TGF-β receptor to form a complex. Receptor-induced phosphorylation of receptor activated Smads (R-Smads) leads to binding to cytoplasmic Smad2/3. Phosphorylated Smads form complexes with Smad4, which are then translocated to the nucleus where they bind to transcription factors that are crucial for gene expression of TIMP-3 and Bcan. *Bcan*, brevican; CA1, CA1 region of the hippocampus; CSPG, chondroitin sulfate proteoglycan; ECM, extracellular matrix; PNN, perineuronal net; RSC, retrosplenial cortex; VGLUT1, vesicular glutamate transporter 1. immunoglobulin G, IgG; Mmp2, Matrix metallopeptidase 2; TIMP-3, Tissue inhibitor of metalloproteinase 3; TGF-ß1, transforming growth factor beta 1. Created with BioRender.com.

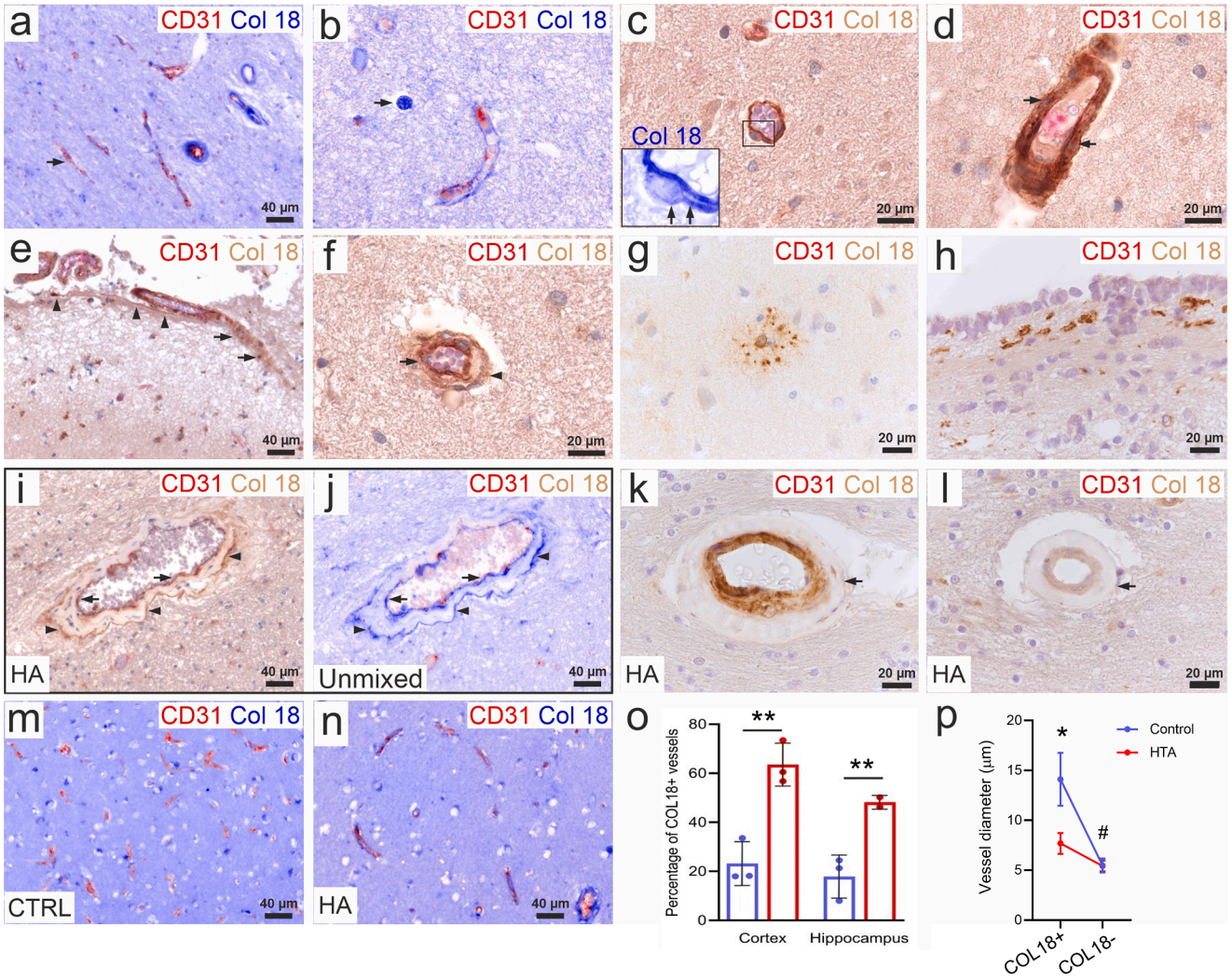

Fig. 10. Collagen XVIII/CD31 staining patterns in patients with cerebral hypertensive arteriopathy and controls. (a) Unmixed low power example of vessels positive for CD31 only (arrow), while the rest have at least some patchy peri-endothelial staining for COL18. (**b**) Unmixed capture showing a double positive capillary and an astrocyte-like nucleus positive for COL18 (arrow). (**c**) Arteriole showing COL18 positivity in a pericyte on the abluminal surface of the vessel [(arrows in the unmixed image (inset)]. (**d**) Artery showing intense COL18 staining in both endothelium and smooth muscle cells (arrows). (**e**) Penetrating pial artery shows strong COL18 positivity in the smooth muscle cells (arrows), with external glia limitans being also positive (arrowheads). (**f**) Arteriole with intense COL18 positivity in the endothelium (arrow) and smooth muscle cells, as well as moderate staining of the perivascular glia limitans (arrowhead). (**g**) Dystrophic-like astrocytic processes with a dense dotted appearance together with patch nuclear staining. (**h**) Dystrophic neuritic-like dense staining under the ependymal cells. (**i-j**) RGB and unmixed venule with COL18 clearly stained endothelium (arrows) and perivascular glia limitans (arrowheads). (**k**) Hyalinized arteriole with intense COL18 staining in tunica media, loss of endothelium (CD31), thickened hyalinized external media, and with a loss of staining in glia limitans (arrow). (**l**) Another hyalinized arteriole with loss of endothelium (CD31) and fainter COL18 staining in the inner tunica media, and with loss of expression in glia limitans (arrow). (**m**) All CD31+ blood vessels are negative for COL18 in an exemplary image from control patients, while (**n**) in many areas, most vessels (CD31+) were also COL18+. (**o**) There are significantly more numerous COL18+ vessels in hypertensive patients group (HTA) for both cortex and hippocampus regions. The mean ± SEM and individual values are shown, ** $p < 0.01$, post hoc Dunn-Sidak test. (**p**) These vessels have reduced diameters in HTA patients and COL18+ are larger than COL18- vessels in the control group. * $p < 0.05$ for comparison between Control and HA groups, # $p < 0.05$ for comparison between COL18+ and COL18- vessels in the HTA group, post hoc Dunn-Sidak test.

identified sharp dystrophic-like neurites or astrocytic processes running in the close vicinity under the ependymal cell layer (Fig. 10 h).

In patients with cerebral hypertensive arteriopathy, for some larger venules with collagenosis-like changes in the tunica media, the reduced amount of smooth muscle cells translated into an overall decrease of COL18 expression by the middle layer, although the endothelium and the internal glia limitans maintained a strong expression (Fig. 10 i, j). Arteriolosclerotic vessels showed massive replacement of tunica media with hyaline, and here we found a variate degree of signal loss in the endothelium and smooth muscle cells, almost always with a complete loss of staining for the internal glia limitans (Fig. 10 k, l). Overall, the number of blood vessels containing at least some endothelial or abluminal COL18 staining was clearly lower in control brain tissue compared to hypertensive patients (Fig. 10 m, n).

A nested MANOVA showed significant effects of Diagnostic Group, Diameter and Region on COL18 immunopositivity (COL18+) of small vessels (**Suppl. Table 2**). In detail, compared to controls, in patients with cerebral hypertensive arteriopathy COL18+ vessels were more frequent, particularly in the cortex compared to the hippocampus (Fig. 10 o & p). Using four-way repeated ANOVA with Region as the repeated measure and Diagnostic Group, Region, and Patient (nested within Phenotype) as additional factors, we detected no effect of Region on the vessel diameter and hence excluded this factor. Using three-way repeated ANOVA, COL18+ vessels were found to be significantly larger than COL18-negative ones ($p < 0.0001$), and there was a significant interaction between the Diagnostic Group and Vessel type ($p = 0.029$),

so the difference in diameters of COL18+ and COL18- vessels was more prominent in the control group (Fig. 10 p).

Discussion

We demonstrated that *Col18a1* deficiency in constitutive Col18a1 knockout mice results in microvascular pathology, i.e. BBB leaks and endothelial activation without microhemorrhages, comparable to early-stage vascular risk-factor related (i.e. hypertensive) sporadic CSVD. Analysis of autopsy brain tissue of patients with cerebral hypertensive arteriopathy/CSVD underpinned the involvement of COL18 in (micro) vascular wall pathology and remodeling. In mice, BBB leaks were accompanied by activation of glial cells, (peri)vascular ECM remodeling and multiple changes in inhibitory and excitatory neuronal circuitries. Disorganization of perineuronal and perisynaptic forms of ECM, which play an essential role in controlling synaptic efficacy and plasticity in these circuitries, became evident. In summary, our study provides evidence that *Col18a1*$^{-/-}$ mice could serve as a model for early vascular risk-factor-related sporadic CSVD, which is particularly useful for investigating resistance and resilience mechanisms for CSVD initiation, progression and clinical manifestation.

Collagen XVIII deficiency and microvascular pathology

Our work was prompted by a study by Moulton and colleagues showing a two-fold increase of albumin-bound Evans blue dye permeability in the aorta and small blood vessels in the skin of *Col18a1*$^{-/-}$ and *Col18a1*$^{+/-}$ mice under normal conditions and in the presence of hypercholesterolemia [50]. The occurrence of COL18 at the fibrillar matrix interface is suggestive of an anchoring function, and consequently, the lack of this collagen entails loosening of the basement membranes.

Our data revealed increased BBB permeability for mouse IgG in the deep gray matter in 5-month-old *Col18a1*$^{-/-}$ mice, accompanied by brain-wide intravascular erythrocyte accumulation in capillaries and arterioles. BBB permeability in RSC and the hippocampus further increased with aging in 12-month-old *Col18a1*$^{-/-}$ mice, whereas the frequency of intravascular erythrocyte accumulation did not change. Increased BBB permeability in *Col18a1*$^{-/-}$ mice might be linked to endothelial TJ protein (*Ocln, Zo1*) downregulation (through IL-1β elevation) or cleavage (*Mmp2* upregulation), or to structural deficits of the BM in the absence of COL18A1 [51,52]. IL-1β elevation also is known to promote astrocytes to release vascular endothelial growth factor, which increases BBB permeability [53].

In line with our results, accumulations of erythrocytes were described to be the first histological peculiarity of CSVD in hypertensive rats, where they are thought to reflect endothelial cell injuries/dysfunction and where they were associated with further CSVD features, i.e. BBB leaks, blood flow reduction and thrombus formation [26,54,55]. Endothelial cell dysfunction is key in the pathogenesis of CSVD, occurring even prior to BBB breakdown [56]. Endothelial dysfunction is thought to be distinct from, but linked to, endothelial activation, which is defined by the increased expression of adhesion molecules such as VCAM-1, ICAM-1, and E-selectin, typically occurring in response to inflammatory stimuli and hypertension [57] and according to our results also can be induced by the *Col18a1* deficiency. VCAM-1 interacts with integrin receptors, adheres to erythrocytes (with subsequent risk of impaired hemodynamics and thrombus formation) and regulates both leukocyte and neuronal function; in humans it was found upregulated in ischemic stroke or AD [58–60]. As COL18A1-derived endostatin reduces the expression of *Vcam1*, VCAM-1 upregulation could be linked to endostatin deficiency and erythrocyte aggregation in *Col18a1*$^{-/-}$ mice [61].

Collagen XVIII deficiency and vascular ECM remodeling

Col18a1$^{-/-}$ mice showed increased both mRNA and protein levels of TGF-ß1 and BM ECM proteins such as *Col3a1, Col4a1, Col8a1*, and *Nid1*, as well as enhanced *Loxl2* expression, which enzymatically crosslinks collagen, overall probably indicating subtle BM/early vessel wall remodeling. Astroglial overexpression of TGF-ß1 has been reported to induce an increased deposition of ECM components in the CNS, particularly around blood vessels, along the glial limitans, as well as on neuronal cell bodies and processes [62]. Moreover, a leak of plasma fibrinogen into the brain parenchyma (Suppl. Fig. 2) may strongly drive the TGF-β signaling in astrocytes [63]. Astroglial TGF-β overexpression contributes to progressive functional decline after stroke and induces CSVD with typical BM thickening, capillary degeneration and string vessel formation, which can be also found in AD patients [62,64–66]. Nidogen-1 and −2 are sulfated monomeric glycoproteins that interact with a range of ECM proteins, in particular laminins, collagen type IV, and perlecan, whose accumulation results in a thick vascular BM. The observed overexpression of *Tgfb1, Col3a1, Col4a1, Col8a1*, and *Nid1* in *Col18a1*$^{-/-}$ mice is thus consistent with characteristic changes seen in CSVD, i.e. neuroinflammation and BM/vessel wall remodeling. Our findings in the human autopsy cohort indeed mirror vessel remodeling with collagen increase, vascular wall thickening and stenoses, typically observed in longstanding risk-factor-related CSVD.

Collagen XVIII deficiency does not lead to enlarged PVS

Enlarged PVS is a feature of early CSVD, which is also evident in aging and several neurological diseases. PVS enlargement might point towards impaired drainage of toxic metabolites or immune cells out of the brain [1,67,68]. We did not observe enlarged PVS in our animal model, similar to previous studies in genetic CSVD, i.e. cerebral autosomal recessive arteriopathy with subcortical infarcts and leukoencephalopathy (CARASIL) [69].

Interestingly, *Aqp4*, a key water channel in astrocytic feet processes that is critical for drainage function, is overexpressed in *Col18a1*$^{-/-}$ mice. This could have contributed to the prevention of PVS pathology [70,71]. Additionally, increased mRNA and protein levels of *Pdgfrb*, which is considered a marker of BBB-associated pericytes, could have played a role in maintaining drainage and thus hindering PVS enlargement [75–77]. However, immunohistochemical analysis of small vessels did not confirm upregulation of PDGFRβ and AQP4. In this context is noteworthy that PDGFRβ is also expressed on fibroblasts in most adult organs under normal conditions [70]. Additionally, PDGFRβ immunoreactivity was observed in NG2^{+} and GFAP^{+} cells within the brain parenchyma [71]. This broad expression pattern may limit our conclusion that pericytes are the source of increased PDGFRβ in our animal model. Additional markers and techniques are needed to confirm alterations in pericytes of *Col18a1*$^{-/-}$ mice.

Collagen XVIII upregulation in human hypertensive brain vasculature

Most interesting, our human autopsy data revealed an increase in vascular Col18 expression in patients suffering from cerebral hypertensive arteriopathy/CSVD. Remodeling of the small vessel walls in the brains of hypertensive patients, which, for example comprise endothelial dysfunction, increased BBB permeability, arteriolar wall thickening, hyaline arteriolosclerosis, or microhemorrhages, occur usually years after longstanding exposure. The longer patients have high blood pressure, the more likely they will develop CSVD [72]. Increased overall deposition of ECM proteins – particularly collagen and fibronectin - in the vascular BM and expansion to other vessel wall structures, e.g. after proliferation and migration of fibroblasts from the adventitia into the media, together with elastin deficiency, are adaptive processes. These adaptations reduce the mechanical (i.e. hypertensive) stress on the vessel wall, maintan BBB integrity and protect the downstream vasculature from increased blood pressure [73].

Comparing our data in *Col18a1*$^{-/-}$ mice against humans show that the relationship between vascular pathology and COL18 expression

levels is clearly related to both, loss-of-function and gain-of-function conditions. The latter particularly plays a role in case that increased collagen expression is a part of an extensive widespread "compensatory" remodeling of the vascular wall, certainly in face of longlasting arterial hypertension [74].

Collagen XVIII deficiency and activation of glial cells

In *Col18a1*$^{-/-}$ mice, glial cells showed several features of activation, e.g. microglia were less ramified with enlarged somata and were found near blood vessels, and astrocytes exhibited higher protein levels of the activation marker GFAP. It is known that microglia display an activated and phagocytotic phenotype in response to BBB breakdown [75]. These morphological and functional changes in activated glial cells are accompanied by the release of chemokines and cytokines and changes in surface antigen expression [76,77]. q-PCR analysis showed upregulated expression of the microglial/macrophage markers *Iba1, Cd86, Mpo, Il1b, Ccl2* and astrocytic *Gfap* in *Col18a1*$^{-/-}$ mice. A recent study demonstrated that IL-1β stimulated astrocytes to secrete proinflammatory chemokines such as CCL2, CCL20, and Chemokine (C-X-C motif) ligand 2 CXCL2, which induce the migration of immune cells such as neutrophils, monocytes, macrophages, dendritic cells, and pathogenic T cells, further disrupting the BBB and causing neuroinflammation [78]. CCL2 further activates and recruits microglia to areas of damage [79], which might provide a mechanism for the recruitment of microglial to leaky blood vessels in *Col18a1*$^{-/-}$ mice**.** Increased CCL2 levels were found in hypertensive patients, where they correlated with hypertension-associated organ damage, and in AD patients, where they predicted cognitive decline in early disease [80]

Microglial cell processes are highly dynamic: they constantly monitor the normal brain, participate in ECM remodeling and removal of dysfunctional synapses, and provide trophic factors to neurons, thereby supporting the plasticity of neuronal connectivity [81]. C1q is the recognition component of the classical complement pathway multisubunit complex. A previous study showed that C1q synthesis is increased at an early age in AD mouse models (i.e., in the absence of fibrillar amyloid plaques) [82]. The present study demonstrates upregulation of C1q protein deposition without changes in *C1q* gene expression in the CA1 and RSC regions of *Col18al*$^{-/-}$ mice, which may be the cause of the synaptic changes described below. We also found a decline in microglial *TREM2* mRNA levels in *Col18al*$^{-/-}$ mice. This may be of functional importance as previous studies have shown that loss of TREM2 increases the risk of AD [83] and TREM2 overexpression attenuates neuronal loss and promotes behavioral improvement in 5xFAD and APP/PS1 models [84,85].

Microglial activation may promote the activation of astrocytes. Activated microglia secrete high levels of TNF-α and IL-1α/β, which convert quiescent astrocytes into the A1 type [86]. Upon activation, A1 astrocytes produce a high level of intermediate filaments GFAP and vimentin [86]. According to IHC staining, we found an increase in GFAP area and intensity as morphological hallmarks of activation. In addition, overexpression of *S100a10* also suggests an increase in the A2 population of astrocytes [87], which are associated with neuroprotection and tissue repair, pointing at the same time to compensatory mechanisms. It remains to study in our model if A1 and A2 populations of astrocytes co-localize or spatially separate, for instance, according to different stages of BBB damage.

Col18a1 knockout and remodeling of perineuronal and perisynaptic ECM

The ECM of PNNs around PV^{+} interneurons and perisynaptic ECM on principal cells is composed of lecticans (Acan, Bcan, Ncan and Vcan). Lecticans are known to be cleaved by MMP9, ADAMTS4/5 and CTSS. We found that 36 % of the PV^{+} interneurons in the CA1 of *Col18a1*$^{-/-}$ mice lack Acan^{+} PNNs. Additionally, the mean intensity of Acan expression was reduced in PV^{+} Acan^{+} cells. Since PNNs control excitability and synaptic inputs to perisomatic interneurons [88], which synchronize neuronal activity and control gamma oscillations, our findings of loss of Acan in PNNs could be a potential source for a certain phenotype, i.e. cognitive deficits, in *Col18a1*$^{-/-}$ mice. This needs to be studied in the future. Reduction in Acan correlated with increased mRNA levels of *Adamts4* and *Ctss*. The upregulated expression of these proteases has been reported in pathological conditions such as AD, ischemic stroke, amyotrophic lateral sclerosis, and spinal cord injury [89–91], but their role in CSVD remains to be investigated. Since *Adamts4* may cleave Vcan deposited in the vasculature, it is possible that upregulation of *Adamts4*, possibly secreted by activated microglia, may contribute to both the opening of the BBB and defects in PNNs and PV^{+} interneurons under different conditions, including CSVD. However, no changes at the ADAMTS-4 protein level were observed in *Col18a1*$^{-/-}$ mice, which points to the regulation of its activity and/or to the potential role of cathepsins in vascular and PNN remodeling [92]. Furthermore, neuroinflammation caused by hypoxia activates microglia/macrophages to release proteases and free radicals that perpetuate the damage over time to ECM molecules and the neurovascular unit (NVU). MMPs secreted by microglia/macrophages in an attempt to remodel the blood vessel wall may have the undesired consequences of opening the BBB and attacking myelinated fibers [93] and Acan+ PNNs.

On the other hand, we found elevated accumulation of Bcan in *Col18a1*$^{-/-}$ mice in the neuropil in general and at perisynaptic sites specifically. In a mouse model of AD-like pathology, increased levels of Bcan and other CSPGs were paralleled by impaired long-term potentiation and contextual memory [94]. The accumulation of Bcan in the ECM was associated with enhanced gene expression of proteins stabilizing interactions between lecticans and hyaluronic acid (*Hapln4),* cross-linking lecticans (*Tnr)* [95] and preventing proteolytic cleavage of lecticans by ADAMTS4/5 (*Timp3*). Notably, the upregulation of TIMP-3 was observed in the CADASIL variant of CSVD, and the knockout of TIMP-3 was proven to reduce the pathological burden of CADASIL [96]. Using the human brain single-cell vascular transcriptome atlas [97], we noticed a downregulation of *Col18a1* in pericytes and an upregulation of TIMP-3 by endothelial cells and perivascular fibroblasts in AD patients, which is in line with our findings in *Col18a1*$^{-/-}$ mice.

In summary, opposite alterations in the perineuronal and perisynaptic ECM have been identified in *Col18a1*$^{-/-}$ mice, which calls for further detailed analysis of the spatial pattern of changes in the expression of lecticans and proteins regulating their stability and proteolytic modifications.

Col18a1 knockout and defects in glutamatergic synapses

Previous findings suggest that a loss and modification of glutamatergic synapses is a correlate of cognitive impairment in both VaD and AD [98–100]. As a universal aspect of the pathological changes associated with dementia, synaptic decline has been demonstrated to be the most accurate correlate of AD severity [101]. Synapse damage occurs also in the early stages of VaD, and the degree of damage is related to the degree of cognitive impairment. The results from our study showed a significant decline in presynaptic VGLUT1 mean intensity in the CA1 region, while VGLUT2 levels remained unchanged. As VGLUT1 and 2 are preferentially expressed in different axonal projections, these data imply that they have different sensitivity to vascular damage. Similar to VGLUT1, we detected a reduction in the expression of the glutamatergic postsynaptic scaffold protein Homer1. It has also been reported that oxidative stress and inflammation of cerebral microvessels caused by hypertension are related to the downregulation of Homer1 [102]. However, no changes in the number of VGLUT1 puncta were detected, suggesting that *Col18a1*$^{-/-}$ mice exhibit synaptic modifications rather than a loss of excitatory synapses. Previous studies have shown that VGLUT1 and VGLUT2 levels significantly change following transient global cerebral ischemia [103], and a reduction in VGLUT1 has been correlated with cognitive performance in VaD patients [98].

Moreover, a previous study in a mouse model of AD showed that fibrinogen at sites of vascular injury promotes spine loss and cognitive decline through a pathogenic microglial response [75]. It remains to be investigated whether the found synaptic changes are related to the upregulation of perisynaptic ECM and/or other neuroinflammatory aspects, including upregulations of IL-1β and increased deposition of C1q/fibrinogen, which serves as a critical cue controlling the outcome of interaction between microglia and synapses.

TGF-ß1/Smad3 signaling plays a role in ECM alterations in Col18a1$^{-/-}$ mice

Correlating with upregulated levels of perisynaptic ECM molecules and TIMP-3 in *Col18a1*$^{-/-}$ mice, we found increased mRNA and protein levels of TGF-β1. TGF-β has been reported to play a major role in the regulation of CSPG expression and secretion from astrocytes [104]. TGF-β-induced expression of CSPG core proteins is mediated by both canonical Smad signaling pathways [105] and also by non-Smad mediated activation of the PI3K–Akt–mTOR signaling pathways [106]. The TGF-β/Smad signaling pathway is essential for vascular development and homeostasis in the brain, and dysfunction of this pathway has been associated with various cerebrovascular disorders [107–109]. TGF-β signaling regulates the formation and permeability of the BBB by controlling tight and adherens junctions [110]. Recent studies have shown that broken BBB in aging humans and rodents is linked to hyperactivation of TGF-β signaling in astrocytes [111]. Conditional genetic knockdown of astrocytic TGF-β receptor-coding genes or pharmacological inhibition of TGF-β signaling rescues the phenotypes in aged mice [112]. Several pathogenic gene variants in the TGF-β pathway have been identified through genome-wide association studies (GWAS) and whole exome trio sequencing. These variants are linked to small vessel ischemic strokes, intracerebral hemorrhages, and sporadic brain arteriovenous malformations (AVMs) [113,114]. Increased expression of TGF-β1 has been found in the brain tissue after ischemic stroke, as well as in hereditary amyloidosis-Dutch type with cerebral hemorrhage [115]. The Smad3 pathway is a downstream mediator of TGF-β signaling and is involved in regulating various cellular processes, including cell growth, differentiation, and apoptosis. A recent study has shown that TGF-*β*1 is driving BBB permeability via downregulation of claudin-5 and upregulation of MMP9 and that these effects are dependent on Smad3 activation [116]. Smad3 activation is also implicated in the production of MMPs and inflammation [117]. These data and our findings highlighting the upregulation of signaling through the TGF-ß1/Smad3 cascade suggest the possible involvement of TGF-ß1 in vascular and

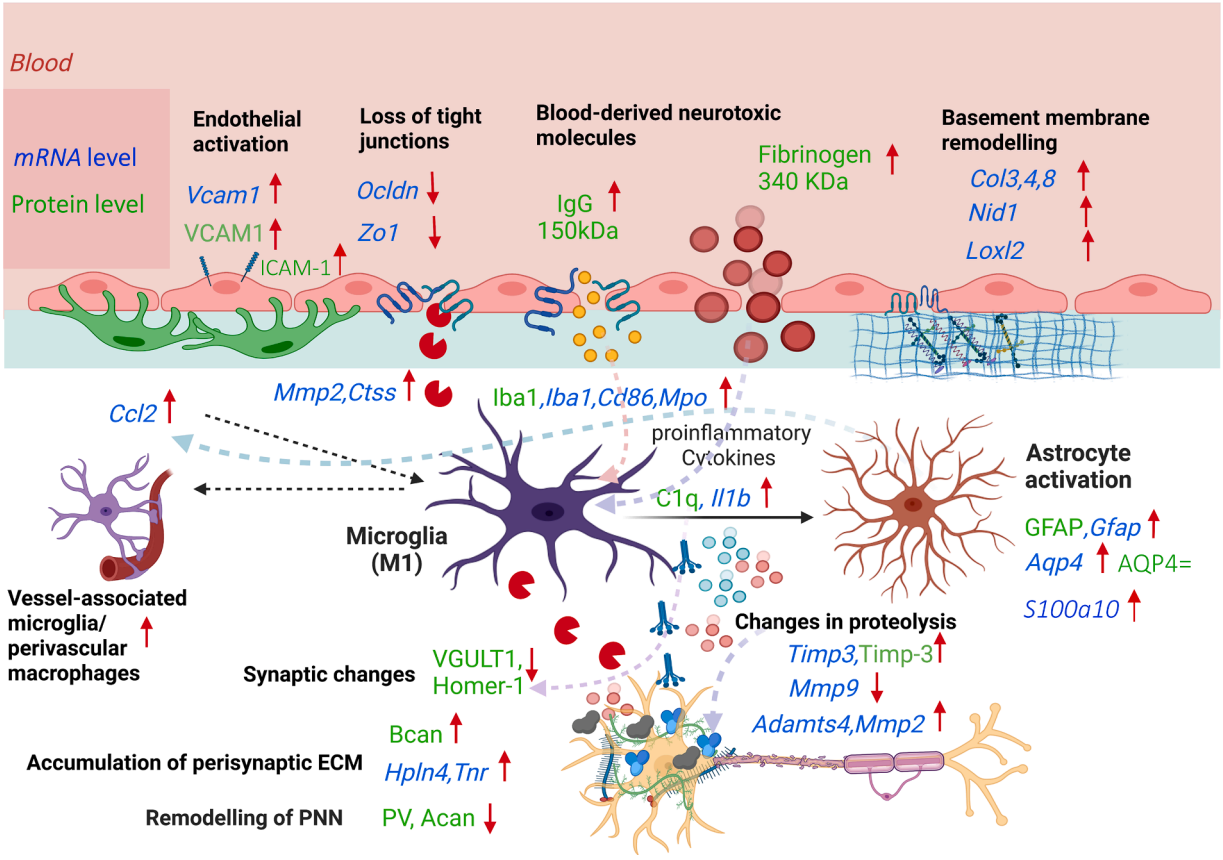

Fig. 11. Summary of findings in *Col18a1*$^{-/-}$ mice. In the absence of collagen XVIII, a variety of changes occur, including the activation of endothelial cells, the remodeling of the basement membrane and impaired function of tight junctions that leads to the CNS entry of blood-derived neurotoxic molecules. BBB damage promotes microglial activation. Activated microglia secrete C1q, IL-1β, MMP2 and CTSS. MMP2 and CTSS may contribute to further degradation of junctional proteins, enlarging the gap between endothelial cells. Following the activation of astrocytes by IL-1β and TGF-β, reactive astrocytes secrete CCL2, which stimulates the migration and recruitment of microglia/perivascular macrophages to damaged vessels. Changes in the expression of proteinases and their tissue inhibitors result in remodeling of PNNs, perisynaptic ECM and C1q accumulation, and synaptic modifications. Alterations in protein levels are represented by green, and alterations in gene levels are represented by blue. *Aqp4,* aquaporin 4*; Adamts4,* a disintegrin-like and metallopeptidase with thrombospondin type 1 motif,4*;* Acan, Aggrecan*;* Bcan, Brevican*; Col3a1,* collagen 3 alpha 1; *Col4a1*, collagen 4 alpha 1; *Col8a1*, collagen 8 alpha 1; *Cldn5*, claudin 5; *Ccl2*, (C—C motif) ligand 2; *C1q,* complement component 1q; *Gfap*, glial fibrillary acidic protein; *Hapln4,* hyaluronan and proteoglycan link protein 4; Iba1, ionized calcium-binding adapter molecule 1; *Il1b,* interleukin 1 beta; *Loxl-2*, lysyl oxidase homolog 2; *Mmp2,9*, Matrix metallopeptidase 2,9; *Mpo,* myeloperoxidase; *Nid1*, nidogen1; Ocln, occluding; *Pdgfrb,* platelet-derived growth factor receptor beta; PV, Parvalbumin; *Tnr,* Tenascin-R; *Timp3,* Tissue inhibitor of metalloproteinase 3; *Vcam1*, vascular cell adhesion molecule 1; VGLUT1, vesicular glutamate transporter 1; *Zo1*, zonula occludens-1. Created with BioRender.com.

synaptic dysfunction in *Col18a1*$^{-/-}$ mice.

Conclusions

Our study uncovered several hallmarks of CSVD in *Col18a1*$^{-/-}$ mice (Fig. 11), namely i) erythrocyte aggregation in capillaries and arterioles, ii) BBB opening, (iii) increased expression of BM proteins, (iv) activation of microglia and astroglia, (v) downregulation of ECM of perineuronal nets, (vi) dysregulation in expression of neural ECM genes and extracellular proteolysis resulting in accumulation of perisynaptic ECM and (vii) reduced expression of key pre- and postsynaptic molecules. Several molecular mechanisms underlying and linking these changes have been highlighted. The upregulation of perisynaptic ECM suggests that treatments targeting ECM, in particular, TIMP-3, could be of relevance for the prevention and therapy of CSVD. As none of the *Col18a1*$^{-/-}$ mice displayed hallmarks typical of advanced CSVD stages, such as hemorrhages, this model could be instrumental in dissecting resistance/resilience factors preventing CSVD progression.

Experimental procedures

Gene targeting and generation of mutant mice

The generation of *Col18a1*$^{-/-}$ mice (B6.129S4-Col18a1tm1Hms; http://www.informatics.jax.org/allele/MGI:2179134) has been described. The strain was maintained through backcrossing heterozygous *Col18a1*$^{+/-}$ mice to the C57BL/6 J mouse strain (Jackson Laboratory) for more than 15 generations and the C57BL/6JOlaHsd strain (Harlan) for more than 10 generations and 4 times with the C57BL/6NCrl strain (Charles River), and heterozygous *Col18a1*$^{+/-}$ matings. Wild-type littermates (*Col18a1*$^{+/+}$) were used as controls in all the experimental analyses. The mouse genotypes were confirmed by polymerase chain reaction (PCR) as described previously [118]. Two cohorts were used: one was perfusion-fixed for histological analyses, and the second cohort was used for both histological and q-PCR analyses as described below.

Tissue collection

Tissue preparation for hematoxylin and eosin staining and immunohistochemistry

For tissue preparation, animals were injected s.c. with fentanyl (0.6 mg/kg body weight), midazolam (15 mg/kg body weight) and medetomidine (2.25 mg/kg body weight) in 0.9 % NaCl solution and then transcardially perfused with phosphate buffered saline (PBS), followed by 4 % paraformaldehyde containing PBS (pump speed of 15 ml/min, duration 240 s each). The following day, the tissue was transferred through PBS washes from PFA to 30 % sucrose in PBS for overnight cryoprotection, frozen in methylbutane (Carl Roth GmbH + Co. KG, Karlsruhe, GER) and stored at −80 °C until sectioning. Coronal slices (thickness 30 μm) of the whole brain were prepared using a cryostat and stored in cryo-protection solution (25 % ethylene glycol, 25 % glycerin, 50 % 0.1 M PBS pH 7.4) at 4 °C. From the frontal to the occipital pole, 3 brain slices were taken from each of the 6 sectional planes with a distance of 750 μm between each sectional plane (18 brain slices per animal in total) for hematoxylin and eosin (HE) staining and immunohistochemistry (IHC) analysis. In this study, HE analysis was performed on sections from 7 wild-type (*Col18a1*$^{+/+}$) and 5 *Col18a1*$^{-/-}$ 5-month-old mice as well as from 5 *Col18a1*$^{+/+}$ and 6 *Col18a1*$^{-/-}$ 12-month-old mice. Furthermore, IHC analysis was performed on sections from 6 *Col18a1*$^{+/+}$ and 5 *Col18a1*$^{-/-}$ 5-month-old mice and 5 *Col18a1*$^{+/+}$ and 5 *Col18a1*$^{-/-}$ 12-month-old mice.

Tissue preparation for qPCR and western blot analysis

After an overdose with i.p. injection of ketamine (75 mg/kg body weight), xylazine (10 mg/kg body weight) and acepromazine (3 mg/kg body weight), tissue isolation for quantitative PCR (qPCR) was performed by intracardial perfusion with ice-cold PBS (pump speed of 15 ml/min, duration 70 s), quick decapitation, and dissection of the brain into ice-cold PBS. Left hippocampi from the second batch of animals were stored for only RNA extraction and downstream processing. Six *Col18a1*$^{+/+}$ and 11 *Col18a1*$^{-/-}$ 12-month-old mice were used for qPCR and western blot analysis.

Histology

For HE staining, brain slices were washed with distilled water twice, incubated with hematoxylin (Carl Roth GmbH + Co. KG, Karlsruhe, GER) for 5 min and washed again, followed by bluing under running tap water for 10 min and another rinse with distilled water. Afterward, staining was performed with 1 % eosin solution (Carl Roth GmbH + Co. KG, Karlsruhe, GER) for 40 s. After dehydration with increasing concentrations of alcohol (Rotisol, Carl Roth GmbH + Co. KG, Karlsruhe, GER), slices were finally placed in Xylene (Carl Roth GmbH + Co. KG, Karlsruhe, GER) and mounted with coverslips using Histomount (Fisher Scientific GmbH, Schwerte, GER).

Quantification

The following CSVD hallmarks were quantified in the HE-stained brain slices: (i) nonocclusive erythrocyte thrombi defined as the accumulation of erythrocytes in the lumen of the vessels (subsequently referred to as erythrocyte thrombi) [54], (ii) small perivascular bleeds/microbleeds defined as leakage of erythrocytes out of the vessel, and (iii) enlarged PVS defined as distended, white, nonstained perivascular areas.

Erythrocyte thrombi and small perivascular bleeds were counted in 25 randomly chosen fields of view (FOV) in different brain regions (retrosplenial cortex (RSC), basal ganglia (BG), hippocampal CA1 region, corpus callosum (CC) and thalamus) in both hemispheres. When quantifying, we additionally differentiated between two different types of vessels: (i) capillaries with a luminal diameter < 10 μm and (ii) small vessels defined through a luminal diameter > 10 μm [119]. Small perivascular bleeds were defined as leakage of erythrocytes out of the vessel visible as a collection of red blood cells that appears red-orange in the perivascular parenchyma with size $\leq$200 μm. Additionally, we checked for the occurrence of macrobleeds with size $\geq$200 μm. For statistical analysis, the mean of all FOVs per brain region was calculated.

For PVS measurements, 18 FOV per brain region (see above) were quantified in each animal. In each FOV, all arterioles and the number of arterioles with PVS in the same FOV were counted. Percentages of arterioles with PVS per FOV were then calculated, and mean values per animal were used for statistical analysis.

RNA extraction, cDNA conversion, and qPCR

A total RNA extract was prepared from the frozen hippocampal region using the EURx GeneMatrix DNA/RNA Extracol kit (Roboklon Cat. No. E3750), following the manufacturer's recommendations [120]. Nano-drops were used to measure the yield, purity, and integrity of RNA. Furthermore, the High-Capacity cDNA Reverse Transcription Kit (Cat. 4,368,814) was used for the conversion of 1.5 μg of RNA to cDNA, and then real-time (RT)-qPCR was performed using a TaqMan gene expression array (Cat. 4,331,182) from Thermo-Fisher Scientific using Quant-Studio-5 from Applied Biosystems (Table 1). Overall, 52 genes were analyzed, comprising five chondroitin sulfate proteoglycan (CSPG) genes, namely, aggrecan (*Acan)*, versican (*Vcan*), neurocan (*Ncan*), phosphacan *(Pcan)* and brevican *(Bcan)*, four genes coding for link proteins, hyaluronan and proteoglycan link protein (*Hapln2, Hapln3, Hapln4)* and tenascin-R (*Tnr),* five genes for major metalloproteinases degrading neural ECM proteins, namely, matrix metallopeptidase 2 (*Mmp2),* matrix metallopeptidase 9 (*Mmp9),* cathepsin S *(Ctss),* a disintegrin-like and metalloproteinase with thrombospondin type 1 motif, 4 (*Adamts4),* a disintegrin-like and metalloproteinase with thrombospondin type 1 motif, 5 (*Adamts5)* and four genes coding for

Table 1
Taqman probes used for real-time PCR analysis.

Gene	Full description	Reference Sequence	Sequence (5′ to 3′)
Acan	Mouse_Aggrecan_Mm00545794_m1	NM_007424.2	**Fw** CCCCCCGCGCAGAGCATCCC
			Rv AAGACATTGGAAGAGATCTA
Vcan	Mouse_Versican_Mm01283063_m1	NM_001081249.1	**Fw** GCCTGTTTCCAAGCTTGGGC
			Rv AAAATTCTTCTTTTACTACA
Ncan	Mouse_Neurocan_Mm00484007_m1	NM_007789.3	**Fw** GGAGGCTGCGCCTGGCGTGC
			Rv TTAAAAAAAAAAAAAAAAAA
Pcan	Mouse_PTPRZ1_Phosphocan_Mm00478484_m1	NM_001081306.1	**Fw** AATTCCGCGCCGCTGCGCTG
			Rv AATATAAATATTGCTATTAA
Bcan	Mouse_Brevican_Mm00476090_m1	NM_001109758.1	**Fw** CGCTGTCGCCCGGAACCCGC
			Rv ATTAAACTGCTTTGTACCCA
Hapln2	Mouse_Hapln2_Mm00480745_m1	NM_022031.2	**Fw** AGAAAAGAAAAGGACAGACA
			Rv TACTATAATAAATCCACTTG
Hapln3	Mouse_Hapln3_Mm00724203_m1	NM_178255.3	**Fw** AGGCCATTCAAGATCCCAAA
			Rv TTATTATTATTTTATTTTAC
Hapln4	Mouse_Hapln4_Mm00625974_m1	NM_177900.4	**Fw** GCACTGGCCGCTCAGCAAGG
			Rv ATTAAAGGTGTAAGCCACCA
Tnr	Mouse_TenascinR_Mm00659075_m1	NM_022312.3	**Fw** AGTAAGAGGGGAAAAGAGAG
			Rv AATCATTGTCGTGTAATAAC
Ocln	Mouse_Occludin_Mm00500912_m1	NM_008756.2	**Fw** GGGTGGGGGAAGCGGAGGAC
			Rv AATTTAAATAATGTTTTTGT
Cldn5	Mouse_Claudin5_Mm00727012_s1	NM_013805.4	**Fw** AGTTGGTGTAGTTAAAACCT
			Rv GTTTGAACACTTTCAAAAAA
Zo1	Mouse_Tjp1_Mm01320638_m1	NM_001163574.1	**Fw** GTGGCCGCCTGAGTTGCCCG
			Rv ACAAAAAAAAAAAAAAAAAA
Lama5	Mouse_Laminin, alpha5_Mm01222029_m1	NM_001081171.2	**Fw** ACTTGCCGGGCTCCTGCGGT
			Rv TTGAAAAAAAAAAAAAAAAA
Nid1	Mouse_Nidogen1_Mm00477827_m1	NM_010917.2	**Fw** GGGAGGTGAGGAGGGACTGC
			Rv AAAATAAAATCTTATTTTGA
Col3a1	Mouse_Collagen, typeIII, alpha 1_Mm00802300_m1	NM_009930.2	**Fw** GGATGGGTTCTGCTCTCATA
			Rv TAAAATATCATAATGAAACA
Col4a1	Mouse_Collagen, type IV, alpha 1_Mm01210125_m1	NM_009931.2	**Fw** TTGGAGACGCCGCCCGCGCA
			Rv AAAAAAAAAAAAAAAAAAAA
Col8a1	Mouse_Collagen, type VIII, alpha 1_Mm01344184_m1	NM_007739.2	**Fw** AAGTGCAAGTTACCCGCAGA
			Rv TAAATATCTCTAAAAATATG
Vcam1	Mouse_Vascular cell adhesion molecule 1_Mm01320970_m1	NM_011693.3	**Fw** GCCCTTTCGGAGCTGAAGGT
			Rv AATACAGATACTCGAAACAT
Loxl2	mOUSE_Lysyl oxidase-like 2_Mm00804740_m1	NM_033325.2	**Fw** GTCTCACTTTGCCCGGGTCC
			Rv AACTCTCTGCTTTAAAAAAA
Mmp2	Mouse_Matrix metallopeptidase 2_Mm00439498_m1	NM_008610.2	**Fw** CCAGCCGGCCACATCTGGCG
			Rv AAAAAAAAAAAAAAAAAAAA
Mmp9	Mouse_ Matrix metallopeptidase 9_Mm00442991_m1	NM_013599.3	**Fw** TGCAAAGGCAGCGTTAGCCA
			Rv AAATGAATATTTACTTATTT
Ctss	Mouse_Cathepsin S_Mm01255859_m1	NM_001267695.2	**Fw** TTCCTCATTGTGGATGCTTC
			Rv TCTGTCATTTCAAATATCTA
Adamts4	Mouse_ a disintegrin-like and metallopeptidase with thrombospondin type 1 motif,4_Mm00556068_m1	NM_172845.2	**Fw** GGGGAGAACCCGGGGAAGAC
			Rv GAACTAGCATAGAGCCTCTC
Adamts5	Mouse_ a disintegrin-like and metallopeptidase with thrombospondin type 1 motif,5_Mm00478620_m1	NM_011782.2	**Fw** GAAATTGCCATTGCAGGATG
			Rv GCACAGGAATAAAAATCAGT
Timp1	Mouse_Tissue inhibitor of metalloproteinase 1_Mm01341361_m1	NM_001044384.1	**Fw** AGGCTTTGACTCCAGCGGTG
			Rv AGCAAAAAAAAAAAAAAAAA
Timp2	Mouse_Tissue inhibitor of metalloproteinase 2_Mm00441825_m1	NM_011594.3	**Fw** CCGGCCTGCACTGGCCGCCA
			Rv AAGAGAAAAAAAAAAAAAAA
Timp3	Mouse_Tissue inhibitor of metalloproteinase 3_Mm00441826_m1	NM_011595.2	**Fw** GCGCCCCCCGGCCCCGCCCC
			Rv AGTGGTTTTATTTCTATCAC
Timp4	Mouse_Tissue inhibitor of metalloproteinase 4_Mm01184417_m1	NM_080639.3	**Fw** GGAGGAGTCCTGGAGGGGCT
			Rv AAGCATTTTCCCTCCAGGTT
Gfap	Mouse_Glial fibrillary acidic protein_Mm01253033_m1	NM_001131020.1	**Fw** CCAGGAAGTCAGGGGCAGAT
			Rv TGCTCCCTGCTCTTCATTTT
Aqp4	Mouse_Aquaporin 4_Mm00802131_m1	NM_009700.2	**Fw** AGTGTACTGGAGCCCGGGGG
			Rv TATATTTGATGGTGTTTAAG
S100a1	Mouse_S100 calcium binding proten A10_Mm00501457_m1	NM_009112.2	**Fw** GTACCCGCCTCGCGTACAAA
			Rv TCCTTTTTTTAAGTTCTGAA
Iba1	Mouse_ Allograft inflammatory factor 1_Mm00479862_g1	NM_019467.2	**Fw** AGACGAACCCTCTGATGTGG
			Rv AATGACGCTCCTAGTGGGTC
Trem2	Mouse_triggering receptor expressed on myeloid cells 2_Mm04209424_g1	NM_001272078.1	**Fw** GCGCCTACCCTAGTCCTGAC
			Rv CAACCCCATTCTCCACACAC
C1q	Mouse_Complement component 1_Mm07295529_m1	NM_007572.2	**Fw** ATGAAACTTGGCAGTGTCCT
			Rv TCCCCGTCTGTGTCTGTGAC
C3	Mouse_complement component 3_Mm01232779_m1	BC029976.1	**Fw** CGGACGCGTGGGGGCTGTTA
			Rv AAAAAAAAAAAAAAAAAAAA
Mpo	Mouse_Myeloperoxidase_Mm01298424_m1	NM_010824.2	**Fw** ATAACTTCTCAGCTTTAGCT
			Rv AAAAAAAAAAAAAAAAAAAA
Cd68	Mouse_CD68 antigen_Mm03047343_m1	NM_001291058.1	**Fw** TTTTAGTTAAGGGAAGTGAG
			Rv AAAACTAAAAAAAAAAAAAA

(*continued on next page*)

Table 1 (*continued*)

Gene	Full description	Reference Sequence	Sequence (5′ to 3′)
Cd86	Mouse_CD86 antigen_Mm00444540_m1	NM_019388.3	**Fw** ATTGCTGAGGAAGAAAGAGG **Rv** TTTTCTTGAATTTTTTCAAG
Cd13	Mouse_Alanyl (membrane) aminopeptidase_Mm00476227_m1	NM_0048486.2	**Fw** GGCAGTGGGGCTCCACCCCC **Rv** TGAAAAAAAAAAAAAAAAAA
Cd47	Mouse_CD47 antigen (Rh-related antigen,integrin-associated signal transducer)_Mm00495011_m1	NM_010581.3	**Fw** CCCGGGCAGCCTGGGCGGCC **Rv** AAAAAAAATCAGAAAAAAAA
Ccl2	Mouse_Chemokine (C—C motif) ligand 2_Mm00441242_m1	NM_011333.3	**Fw** GCAGAGAGCCAGACGGGAGG **Rv** ATATATTATTTTTGTACACC
Tgfb1	Mouse_ Transforming growth factor, beta 1_Mm01178820_m1	NM_011577.1	**Fw** CGCCGCCGCCGCCGCCCTTC **Rv** GGCCCCGCCCCCGCCCCGCC
Plp1	Mouse_Proteolipid protein (myelin) 1_Mm01297210_m1	NM_001290561.1	**Fw** AATCAGAAAGCCCTTTTCAT **Rv** AAATACTTGTCTCAAATTGA
Cspg4	Mouse_Chondroitin sulfate proteoglycan 4_Mm00507257_m1	NM_139001.2	**Fw** GACTTGCGACTTGCGACTCG **Rv** TAAATAAATAAATGCTCCCA
Pdgfrb	Mouse_ Platelet derived growth factor receptor, beta polypeptide_Mm00435553_m1	NM_001146268.1	**Fw** GGGGCAGAGAAAGCCCACAG **Rv** TGCTTCTCACTGAATAACCG
Aca2	Mouse_actin,aplha2, smooth muscle_Mm00725412_s1	NM_007392.3	**Fw** CAAGGGGCTATATAACCCTT **Rv** AATAAAATGTGACAACCGGA
Il6	Mouse_Interleukin 6_Mm00446190_m1	NM_031168.1	**Fw** CCAAGAACGATAGTCAATTC **Rv** AAATAAATTATATTATATTT
Il33	Mouse_Interleukin 33_Mm00505403_m1	NM_001164724.1	**Fw** AGCTCTCCACCGGGGCTCAC **Rv** TCAAAACCACGTGTGACCAC
Il1b	Mouse_Interleukin 1 beta_Mm00434228_m1	NM_008361.3	**Fw** CGAGGCCTAATAGGCTCATC **Rv** ATTTCATTAAAACAAACAAA
Tna	Mouse_Tumor necrosis factor_Mm00443258_m1	NM_001278601.1	**Fw** AGCAGAAGCTCCCTCAGCGA **Rv** CGCTTGGAAAAGAAATGTGA
Abcb1a	Mouse_ P-gp _Mm00440761_m1	NM_011076.2	**Fw** ACAGTGGAACAGCGGTTTCC **Rv** TTAAAAGACCCTAAGGATTC
Icam1	Mouse_intercellular adhesion molecule 1_Mm00516023_m1	NM_010493.2	**Fw** GCGCCGCCCG CCTCAGTCTG **Rv** CTTTCCTTTG AATCAATAAA

tissue metalloproteinases inhibitors *(Timp1, Timp2, Timp3, Timp4)*. In addition, three genes coding for TJ proteins - occludin *(Ocln),* claudin-5 *(Cldn5)* and zonula occludens-1 (*Zo1)* - and six genes coding for basement membrane proteins laminin alpha5 (*Lama5),* nidogen1 (*Nid1),* collagen III alpha 1 (*Col3a1),* collagen IV alpha 1 *(Col4a1),* collagen VIII alpha 1 *(Col8a1)*, vascular cell adhesion molecule 1 *(Vcam1),* intercellular adhesion molecule 1 (*Icam1*), p-glycoprotein 1 (*Abcb1a*) and lysyl oxidase-like 2 *(Loxl2)* were also analyzed. Additionally, the expression of three astrocyte markers, glial fibrillary acidic protein *(Gfap),* aquaporin 4 *(Aqp4), and* S100 calcium-binding protein A10 (*S100a10);* microglial genes, allograft inflammatory factor 1 (*Iba1),*targeting receptor expressed on myeloid cell 2 *(Trem2),* complement component 1 (*C1q),* complement component 3 *(C3)*, myeloperoxidase *(Mpo),Cd68, Cd86, Cd47,* chemokine (C—C motif) ligand 2 (*Ccl2);* transforming growth factor beta 1 *(Tgfb1)*; two oligodendrocyte/oligodendrocyte progenitor cell (OPC) markers, proteolipid protein (myelin) 1 (*Plp1)* and chondroitin sulfate proteoglycan 4 (*Cspg4);* pericyte marker, platelet-derived growth factor receptor, beta polypeptide (*Pdgfrb), Cd13,* alpha smooth muscle *(Asma); and* three interleukins (*Il1b, Il6*, and *Il33*) and Tumor necrosis factor *(Tnfa)* were also quantified and analyzed relative to the expression of glyceraldehyde 3-phosphate dehydrogenase (*Gapdh*). The *Gapdh* gene was used to normalize the expression levels of these genes as a housekeeping gene whose expression was not altered in the compared conditions [121].

Immunohistochemistry

All sections were washed at room temperature (RT) three times with 120 mM phosphate buffer (PB), pH = 7.2, for 10 min each wash, followed by permeabilization with 0.5 % Triton X-100 (Sigma-Aldrich Inc. T9284, St. Louis, MO, USA) in PB for 10 min at RT. The sections were subsequently blocked using a blocking buffer (0.4 % Triton X- 100 + 10 % goat serum (Gibco 16210–064, Amarillo, TX, USA/Thermo Fisher Scientific 16210–064, Waltham, MA, USA) + 0.1 % glycine in PB) for 45–60 min at RT. Afterward, sections were either incubated overnight at 37 °C or for 2 days at 4 °C depending on which primary reagents were used (Table 2). Following three washes with PB, sections were incubated with secondary antibodies (Table 2) for 2 h at RT. Labeled sections were washed again three times at RT for 10 min in PB and mounted on glass slides using Fluoromount medium (Sigma-Aldrich F4680, St. Louis, MO, USA) [122].

SDS-PAGE and western blot analysis

Brain tissue from 12-month-old mice (right cortex) was homogenized by 12 up and down strokes with a motor-operated Teflon-glass homogenizer (0.25 mm clearance), using 1 g (wet weight) brain/4 ml of 5 mM Hepes buffer, pH 7.4, containing 0.32 M sucrose and a protease inhibitor cocktail (Complete; Boehringer Mannheim). The resultant homogenates were diluted to 10 % (wt/vol). For semiquantitative assessment of brevican, chondroitin sulfate side chains were digested by incubating samples with chondroitinase ABC (Sigma-Aldrich, St. Louis, United States) at 0.1 U per 60 μg protein in 40 mM Tris–HCl, 40 mM sodium acetate, pH 8.0, for 90 min at 37 °C. All samples were solubilized in 5 x SDS loading buffer (250 mM Tris/HCl, pH 8, 50 % glycerol, 10 % SDS, 0.25 % bromophenol blue, 0.5 M DTT) and boiled at 95 °C for 10 min. To assess relative differences in total protein concentrations, we run test gels with all samples and stained gels with Coomassie blue, a dye that binds to proteins, allowing visualization and quantification (Suppl. Fig. S3). The total intensity of all Coomassie blue-stained bands was used to adjust protein loading for Western lots. Adjusted sample volumes were separated on 2,2,2-trichloroethanol (TCE)-containing stain-free 5–20 % Tris-glycine SDS polyacrylamide gels under reducing conditions. Before Western blotting proteins were activated under UV light for 5 min. Protein transfer onto PVDF membranes (Merck Millipore, Burlington, MA, United States) was performed according to standard protocols. To control for proper protein transfer, UV images of the membranes were captured. After blocking for 1 h at RT in 5 % horse serum (Sigma-Aldrich, St. Louis, United States) in TBS-T (150 mM sodium chloride, 50 mM Tris, 0.1 % (v/v) Tween20, pH 7.6) membranes were incubated in primary antibodies (Table 3) overnight at 4 °C. After washing three times with TBS-T for 10 min, blots were incubated with secondary antibodies for 60 min at RT. After three more washing steps with TBS-T for 10 min, immunodetection was performed using an ECL Chemocam Imager (INTAS Science Imaging Instruments GmbH,

Table 2
Primary and secondary reagents used for histochemistry.

Reagent or Resource	Dilution	Source	Identifier
Primary reagents			
STL-FITC	1:250	Vector Laboratories, Newark, CA, USA	Cat # FL-1161
Rabbit anti-Iba1	1:1000	Wako, Richmond, VA, USA	Cat# 019–19,741
Chicken anti-GFAP	1:500	Millipore, Boston, MA, USA	Cat#AB5541
Rabbit anti-C1q	1:1000	Abcam, Berlin, Germany	Cat# ab182451
Mouse anti-αSMA Cy3-conjugated	1:200	Sigma-Aldrich, MO, U	Cat# C6198
Mouse anti-AQP4	1:200	Santa Cruz Biotechnology, TX, USA	Cat# sc-32,739
Rabbit anti-PDGFRβ	1:200	Invitrogen, Waltham, MA, USA	Cat# MA5–14,851
Rabbit anti-aggrecan	1:300	Millipore, Boston, MA, USA	Cat# AB1031
Chicken anti-parvalbumin	1:500	Synaptic Systems, Gottingen, Germany	Cat#195,006
Chicken anti-VGLUT1	1:1000	Synaptic systems, Gottingen, Germany	Cat# 135,316
Chicken anti- VGLUT2	1:1000	Synaptic Systems, Gottingen, Germany	Cat# 135,416
Guinea pig anti- VGAT	1:500	Synaptic Systems, Gottingen, Germany	Cat# 131,004
Guinea pig anti-Homer1	1:500	Synaptic Systems, Gottingen, Germany	Cat# 160,004
Rabbit anti-brevican	1:1000	LIN, Magdeburg, Germany	[130]
Rabbit anti-β-Amyloid, rodent specific	1:200	BioLegend, San Diego, CA, USA	Cat# 826,801
Rabbit anti-fibrinogen	1:500	Abcam, Berlin, Germany	Cat# ab92572
Mouse anti-human COL18	1:150	University of Oulu, Finland	DB144-N2 in [129]
Rabbit anti-human CD31/ PECAM-1	1:200	Novus Biological, Centennial, USA	Cat# NB100–2284
Secondary reagents			
Goat anti-rabbit Alexa Fluor 546	1:1000	Invitrogen, Waltham, MA, USA	Cat# A-11,035
Goat anti-rabbit Alexa Fluor 647	1:500	Invitrogen, Waltham, MA, USA	Cat# A-21,245
Goat anti-mouse Alexa Fluor 546	1:500	Invitrogen, Waltham, MA, USA	Cat# A11030
Goat anti-mouse Alexa Fluor 647	1:200	Invitrogen, Waltham, MA, USA	Cat# A-21,236
Goat anti-chicken Alexa Fluor 546	1:1000	Invitrogen, Waltham, MA, USA	Cat# A-11,039
Goat anti-chicken Alexa Fluor 647	1:500	Invitrogen, Waltham, MA, USA	Cat# A21469
Goat anti-rabbit Alexa Fluor 405	1:1000	Invitrogen, Waltham, MA, USA	Cat# A-31,556
Goat anti-Guinea pig Alexa Fluor 405	1:1000	Invitrogen, Waltham, MA, USA	Cat# A-31,553
Goat anti-mouse CF 633	1:500	Biotium, Fremont, CA, USA	Cat# 20,122
ImmPRESS® HRP Goat Anti-Mouse IgG Polymer Detection Kit	Ready to use	Vector Laboratories, Burlingame, CA, USA	Cat# MP-7452
ImmPRESS®-AP Horse Anti-Rabbit IgG Polymer Detection Kit	Ready to use	Vector Laboratories, Burlingame, CA, USA	Cat# MP-5401

Table 3
Primary and secondary reagents used for immunoblotting.

Reagent or Resource Primary reagents	Dilution	Source	Identifier
Rabbit anti-Smad3 (EP568Y)	1:1000	Abcam, Berlin, Germany	Cat # AB40854
Rabbit anti-Smad3 (phosphor S423+S425) (EP823Y)	1:1000	Abcam, Berlin, Germany	Cat# AB52903
Rabbit anti-TGFβ1	1:1000	Abcam, Berlin, Germany	Cat#AB215715
Rabbit anti-VCAM1	1:1000	Abcam, Berlin, Germany	Cat# AB134407
Rabbit anti-TIMP-3	1:1000	Abcam, Berlin, Germany	Cat# AB39184
Rabbit anti-brevican	1:3000	LIN, Magdeburg, Germany	[130]
Rabbit anti-ADAMTS-4	1:1000	Abcam, Berlin, Germany	Cat#AB185722
Rabbit anti-PDGFRβ	1:1000	Abcam, Berlin, Germany	Cat#AB32570
Rabbit anti-Occludin	1:1000	Abcam, Berlin, Germany	Cat# 216,327
Mouse anti-ICAM-1	1:250	Thermo Fisher Scientific, Sunnyvale, CA, USA	Cat# MA5407
Rabbit anti- Claudin-5	1:1000	Abcam, Berlin, Germany	Cat# AB131259
Rabbit anti-GLUT-1	1:1000	Cell signaling-Danvers, MA, USA	Cat# 12,939
Secondary reagents			
Donkey anti-rabbit	1:10,000	Jackson Immuno Research, Cambridgeshire, UK	Cat#711,035,152
Donkey anti-mouse	1:10,000	Jackson Immuno Research, Cambridgeshire, UK	Cat#**715,035,150**

Göttingen, Germany). Quantification of band intensities was done using NHI ImageJ software version 1.52a (US National Institutes of Health, Bethesda, MD, United States).

Immunohistochemical analysis of vascular markers

Coronal hippocampal slices were prepared using a cryostat and stored in cryo-protection solution (25 % ethylene glycol, 25 % glycerin, 50 % 0.1 M PBS pH 7.4) at 4 °C. Selected hippocampi sections were washed three times with 120 mM phosphate buffer solution (PBS), pH = 7.2, for 10 min each wash, at room temperature (RT). For AQP4, STL and GFAP labeling, the sections were subsequently blocked using a blocking buffer for efficient blocking of endogenous mouse IgG (0.4 % Triton X-100 + 10 % goat serum (Gibco 16210–064, Amarillo, TX, USA/Thermo Fisher Scientific 16210–064, Waltham, MA, USA) + 0.1 % glycine + 1:300 goat F(ab) anti-Mouse IgG H&L (ab6668, in PBS)) for 2 h at RT. For PDGFRβ, STL and αSMA labeling, the sections were blocked using a blocking buffer (0.4 % Triton X- 100 + 10 % goat serum + 0.1 % glycine, in PBS) for 60 min at RT. For AQP4, STL and GFAP labeling, the sections were washed four times with PBS and were post-fixed using 2 % PFA solution for 15 min, at RT, washed three times in PBS and subsequently blocked again using the blocking buffer (0.4 % TritonX- 100 + 10 %goat serum + 0.1 % glycine) for 30 min at RT. Following three washes with PBS, sections were incubated with primary antibodies (for 2 days at 4 °C. The sections were washed 3 times in PBS and incubated with secondary antibodies for 3 h at RT. Following three washes, the sections were incubated with 4′,6-diamidino-2-phenylindole (DAPI) for 10 min at RT, thereafter the slices were washed once with PBS and mounted on glass slides using Fluoromount medium (Sigma-Aldrich F4680, St. Louis, MO, USA).

Image acquisition

To analyze the tissue distribution of mouse immunoglobulin G (IgG) in *Solanum tuberosum lectin*-fluorescein isothiocyanate (STL-FITC)-fluorescent small vessels, the expression of vascular ECM markers, astroglial/microglial cell activation, and synaptic puncta, images were acquired using a Zeiss confocal microscope (LSM 700) and EC Plan-Neofluar 20 × /0.50 M27, 40 × 1.3 oil M27 and 63 × /1.40 oil M27 objectives by an experimenter blinded to the experimental groups. The acquisition conditions were maintained throughout all the imaging sessions to compare the fluorescence intensity between samples. Images were further processed and analyzed using the open software ImageJ

(Fiji) [123] and MATLAB 2019a (MathWorks, Natick, MA).

Quantification of IgG leakage as an indicator of BBB breakdown

BBB integrity was assessed by measuring the parenchymal abundance of mouse IgG. Briefly, sections containing the RSC, dorsal striatum (DS), CA1, BG, thalamus, and medial prefrontal cortex (mPFC) from young animals as well as the RSC and CA1 from aged animals were immunostained with anti-mouse IgG antibody and STL-FITC. Accordingly, we calculated the vascular leaks as a percentage of overlap between IgG^+ area and STL^+ relative to the total STL^+ area. To accomplish this, we measured the positive area (in μm^2) represented in each IHC-stained section by using self-developed MATLAB code based on a thresholding technique. Analyses were performed on nine images from each region of each animal.

Quantification of vascular markers

The AQP4 intensity in vessels was measured after outlining the ROIs around blood vessels. These masks were used to eliminate the GFAP signal overlapping with the vessels. Then astrocytes were outlined using the GFAP channel (magic wand function) and the mean AQP4 signal intensity was measured within astrocytic ROIs. Both vascular and astrocytic AQP4 intensities were corrected using the mean AQP4 signal measured in negative control slices. αSMA signal associated with the arterioles was measured after outlining the areas (αSMA mask) where the signal was present (> 20 μm diameter). PDGFRβ intensities were measured in arterioles using αSMA masks and in capillaries (outlined using the STL channel). Measured PDGFRβ and αSMA intensities were corrected using the corresponding mean values from negative control slices.

Vessel-associated microglia/perivascular macrophages

The association of microglia/perivascular macrophages with blood vessels was quantified in fluorescence microscopy images using Fiji by comparing the vessel area associated with microglia and the total area of blood vessels in FOVs located in the CA1 region. To quantify the associated area, we used color thresholding and binary analysis. Manual thresholds were set according to signal intensities. Then, the selected threshold value was applied to all animals, and the resulting data represent the percentage of signal colocalization. Ten random images from each group were analyzed.

Microglia and C1q analyses

It is widely accepted that there are clear morphological changes in microglia after activation, such as enlargement of soma and a reduction of microglial processes [124,125]. Ionized calcium-binding adaptor molecule 1 (Iba1) antibody recognizes the microglial protein Iba1, which is commonly used as a microglia/macrophage-specific marker. For the evaluation of the arborization area, somatic area and number of positive ($Iba1^+$) cells, nine images per animal were acquired. Square regions of interest (ROIs) ($374 \times 374\ \mu m^2$) were selected in the RSC and CA1. Two different thresholding and size exclusion criteria were applied to measure the total area covered by branching (thresholding 1: autothresholding with the mean dark option) and the soma area (thresholding 2: autothresholding with the triangle dark option) of $Iba1^+$ cells. The soma area was subtracted from the total area to calculate the total area covered by Iba1 branching. Thresholding 2 with a size-exclusion parameter enabled us to accurately count the number of $Iba1^+$ cells. Differences in the averaged arborization area and somatic area per cell were calculated and normalized in each animal. The number of $Iba1^+$ cells was counted manually.

For microglial morphology analysis, we also used 3DMorph, a MATLAB-based script that analyzes microglial morphology from 3D data as described elsewhere [126]. Briefly, the program uses graphical user interfaces to initially define an image threshold, noise limits, and cell sizes. The program requires the input of threshold levels, cell size expectations, and preferred methods of skeletonization. After these settings were defined, the program made measurements automatically. The output data included cell volume, territorial volume, branch length, number of endpoints and branch points, and the average distance between cells. For 3DMorph analysis, 3 images per animal were taken in the CA1 region using a Zeiss LSM 700 confocal microscope equipped with an EC Plan-Neofluar, 63 × /1.40 oil M27 objective (16-bit, 12 optical sections, 0.2 μm intervals between sections, 1024 × 1024 pixels, pixel size of 0.625 μm).

For quantitation of C1q expression in the *stratum radiatum* of the CA1 region and RSC, images were analyzed using Fiji software. Three ROIs (squares) were defined randomly within soma-free ROIs, and the mean pixel intensity per ROI was determined. The mean ROI intensity per animal was obtained by averaging all ROI mean intensities in the sections studied (three sections per region).

Astroglia analysis

GFAP antibody has been extensively used to investigate astrocytic activation [127]. To count GFAP-positive ($GFAP^+$) cells, 3 images per animal were taken in the CA1 region using a Zeiss LSM 700 confocal microscope equipped with an EC Plan-Neofluar, 40 × 1.3 oil M27 objective (16-bit, 12 optical sections, 1.2 μm intervals between sections, 1024 × 1024 pixels, pixel size of 0.625 μm). Autothresholding (moments dark option) and size exclusion criteria (size = 20) were applied in Fiji to measure the area and mean intensity of $GFAP^+$ cells on the maximum intensity z-projection images. The number of $GFAP^+$ cells was counted manually.

Neural ECM analysis

To count the perineuronal net (PNN)-associated and parvalbumin (PV)-immunopositive (PV^+) cells, 3 images per animal were taken per RSC and the CA1 region using a Zeiss LSM 700 confocal microscope equipped with an EC Plan-Neofluar, 40 × 1.3 oil M27 objective (16-bit, 12 optical sections, 1.2 μm intervals between sections, 1024 × 1024 pixels, pixel size of 0.625 μm). The soma area and intensity were measured on the maximum intensity z-projection images using Fiji.

Anti-Aggrecan antibodies were used to label the ECM of PNNs Aggrecan antibody labels the Acan core protein [95,128]. The numbers of PV^+ Acan-immunopositive ($Acan^+$) and PV^+ Acan-immunonegative ($Acan^-$) cells were counted manually. For soma size and mean intensity quantification, the somata of PV^+ $Acan^+$ cells were manually outlined, and a band of 1.5 μm was then created as the ROI to measure the mean intensity and soma area of PV cells and the mean intensity of Acan signals. In addition, the somatic areas of $Acan^+$ cells were measured as described.

Presynaptic and synaptic scaffold protein analysis

Previous findings suggest that a loss of glutamatergic synapses and changes in the expression of pre- and postsynaptic proteins are correlates of cognitive impairment in both CSVD and AD [99,100]. To count synapses, 3 images per animal were taken per RSC and the CA1 region using a Zeiss LSM 700 confocal microscope equipped with an EC Plan-Neofluar, 40 × 1.3 oil M27 objective (16-bit, 12 optical sections, 1.2 μm intervals between sections, 1024 × 1024 pixels, pixel size of 0.625 μm). We analyzed the mean ROI intensity and the numbers of presynaptic vesicular glutamate transporter 1 (VGLUT1)- and vesicular glutamate transporter 2 (VGLUT2)-immunopositive puncta in the neuropil area. The expression levels of VGLUT1 and VGLUT2 in the CA1 *stratum radiatum* and RSC were quantified using Fiji software. Three ROIs (squares) were defined randomly within soma-free ROIs, and the mean pixel intensity per ROI was determined. To obtain the mean ROI intensity per animal, three ROI mean intensities in each region were averaged.

Furthermore, we analyzed Homer-1-immunopositive puncta because Homer-1 is a postsynaptic scaffolding protein that regulates glutamatergic synapses and spine morphogenesis. The expression levels of

Homer-1 in CA1 *str. radiatum* and RSC were quantified using Fiji. To determine the mean pixel intensity within each ROI, three random ROIs (squares) were defined within soma-free ROIs, and then three ROI mean intensities were averaged in each region to obtain the mean ROI intensity per animal.

Analysis of VGLUT1^{+} puncta and perisynaptic brevican

To study the synaptic changes in the adult *Col18a1*$^{-/-}$ mouse RSC and CA1 and correlate these changes to the respective perisynaptic ECM, we developed a semi-automatic open-source Fiji script that we named Analysis of PeriSynaptic Matrix (APSM_v1.1) [44]. The program can be applied to confocal z-stacks and prompts the user to choose the sharply focused plane to be used for quantification. The program detects the clusters of high-intensity pixels as presynaptic boutons in a noisy background in brain sections. It further allows filtering out puncta not representing synaptic boutons based on the intensity, size, and circularity of the structures. In contrast to other thresholding methods available in Fiji, we were able to automatically segment presynaptic boutons using this tool and obtained quantification of individual synaptic puncta and the ECM associated with them. We quantified the expression of these proteins in the CA1 *str. radiatum*.

Following the manual selection of the sharpest VGLUT1 signal, the program performs a maximum intensity projection of 3 z-planes (the selected central plane + the planes above and below), subtracts the background and applies a Gaussian filter. Next, it implements the Find Maxima algorithm (prominence = 2 (user-defined)), exclusion of maxima on image edges) to locate local maxima that are the brightest VGLUT1^{+} areas of synaptic boutons and collect the x-y coordinates of these pixels (central pixels).

Furthermore, the program iterates over all the identified central x-y coordinates and finds the pixels nearby to identify surrounding pixels belonging to the same presynaptic bouton according to user-defined criteria of the percentage of intensity of the central pixel within a specified radius. For this study, all neighboring pixels within a 1 μm radius of the central pixel that are at least 75 % as bright as the central pixel are considered to be part of the same bouton. Furthermore, it applies the area (>0.05 μm^2) threshold to filter out nonwell-defined structures. Finally, it measures the properties of the remaining synaptic puncta and measures the mean intensity signals within perisynaptic bands surrounding the synaptic puncta (width = 0.2 μm in this study) in all channels of the original image. The number of puncta was quantified after filtering particles for size (included from 0.3 to 1 μm^2) and circularity (included from 0.5 to 1). Finally, the selection of binarized puncta was used as a mask to measure the fluorescence intensity (FI) of puncta.

Data analysis and statistics for mouse data

Statistical analysis was performed with Prism GraphPad (v.8.3.0). To compare two groups, the *t*-test with Welch's correction was used. To compare multiple groups, ordinary two-way ANOVA with Sidak's multiple comparisons test was used to examine the genotype x age interaction. Two-way RM ANOVA with Sidak's multiple comparisons test was used to assess the genotype x region interaction. All bar graphs represent the mean ± standard error of the mean (SEM), with individual sample values shown as dots. Statistical significance was accepted at $p < 0.05$.

Tissue processing and immunohistochemistry of human tissue

Archived formalin fixed paraffin embedded tissue (FFPE) blocks have been selected from the brain tissue database within the Department of Histology of the University of Medicine and Pharmacy of Craiova – Romania (UMFCV), sectioned as 4 μm-thick serial sections for hematoxylin and eosin staining and for double immunohistochemistry. This brain bank was created before 2010 for studying the histopathology of ischemic and hemorrhage stroke, with written informed consent from each patient or her/his relatives, and approved by the local ethics committee of the UMFCV (02/17.02.2009). We sought available tissue blocks from superior frontal or temporal cortices, and hippocampus (dentate gyrus and the cornu ammonis) from patients diagnosed with microvascular ischemic stroke or hypertensive intracerebral hemorrhages, which all demonstrated with hypertensive pathological vascular changes. Patients with large artery/atherosclerotic occlusive disease, or hemorrhages due to malformations, trauma or tumors have not been considered. All cases had hypertensive-related pathology changes/cerebral hypertensive arteriopathy like microatheroma, arteriolar hyalinization of tunica media and/or fibrinoid necrosis, stasis, microthrombosis, petechial hemorrhages, small cortical/subcortical infarctions. In cases with larger cortical-subcortical infarctions/large hemorrhages only tissue from the contralateral hemisphere was taken into account. Control tissue has been selected from the same database, from patients deceased after non-CNS pathologies, and without identifiable vascular pathology (**Suppl. Table S2**). None of these cases had been diagnosed with dementia prior to death.

After pathology re-confirmation, seriate sections from the three anatomical areas for each patient have been processed for sequential double immunohistochemistry for CD31 and COL18. As we were interested in assessing the vascular expression of COL18, this double staining was utilized to explore both the endothelial/abluminal expression patterns of COL18, and also to compare CD31/COL18 double-positive vessels to CD31-positive / COL18-negative vessels.

Briefly, the sections were deparaffinized in xylene, rehydrated in graded alcohol series, and processed for antigen retrieval by microwaving in EDTA pH 9 for 20 min at 650 W, incubated in 1 % hydrogen peroxide in distilled water for 30 min to block the endogenous peroxidase, kept for another 30 min in 3 % skimmed milk in PBS (Bio-Rad Laboratories GmbH, München, Germany), then incubated with the anti-COL18 antibody at 4 °C for 18 h. Next day, the signal was amplified for 1 h utilizing a goat anti-mouse peroxidase polymer-based system (Vector Laboratories, Burlingame, CA, USA), and detected with 3,3′-diaminobenzidine (DAB) (Vector Laboratories). After thorough washing, the rabbit anti-CD31 primary antibody (Novus Biologicals, Centennial, USA, 1:200) was added to the slides for further 18 h at 4 °C. On the last day, the new signal was amplified with a horse anti-rabbit alkaline phosphatase polymer (Vector Laboratories) for 1 h, and the signal was detected with Fast Red (Vector Laboratories). Finally, the slides have been counterstained with hematoxylin and coversliped utilizing a glycerol-based mounting medium (Dako, Glostrup, Denmark). All slides have been processed at the same time for protocol consistency together with control slides stained either with DAB or Fast Red to obtain pure spectral signatures of the respective stains (see further below). Negative controls were obtained by omitting the primary antibodies.

Image processing and analysis of human samples

In order to identify and evaluate the immunohistochemical expression of CD31 and COL18 even when overlapping, 6–7 random field of views (FOVs) spectral cubes have been acquired from each region utilizing a Nikon Eclipse 90i motorized microscope (Nikon Europe BV, Amsterdam, the Netherlands), under a 40 × objective, through a Nuance FX multispectral camera and using the Nuance analysis software (Perkin Elmer, Hopkinton, MA, United States). After building a spectral library from individual slides stained for either DAB or Fast Red (as described above), we were able to efficiently unmix and characterize the separate immunohistochemical expression patterns of CD31 and COL18 (**Suppl. Fig. S7**). For each FOV, we assessed which vessels showed positivity only for CD31 or for both CD31 and COL18, and measured and recorded their lumens' diameters. After spectral separation, processed FOVs were imported in Image Pro 11 image analysis package (Media Cybernetics, Bethesda, MD, USA), and inner diameters were measured based on the CD31 signal (**Suppl.** Fig. 7 **e**). Raw data were saved in Excel sheets, COL18 +/- vessel densities and diameters have been averaged per FOV, and then per anatomical region and patient. Nested MANOVA and ANOVA tests were utilized to compare multiple groups at $p < 0.05$.

Declaration of competing interest

The authors declare that they have no competing interests.

Data availability

The data supporting the findings of this study are available from the corresponding authors upon request.

Acknowledgments

We are thankful to Katrin Boehm and Kathrin Hartung for expert technical assistance, to Ritva Heljasvaara for mouse breeding cohorts, Taina Pihlajaniemi for mouse samples and anti-human COL18 antibodies, the Oulu Laboratory Animal Centre for good care of the mice, and Melina Westhues for help with the preparation of gels for Western blotting.

Funding

This research was supported by the DFG (362321501/RTG 2413 SynAGE, TP5, TP7, TP8, Squad B and 425899996/CRC1436) and Sigrid Jusélius Foundation and by funds from the German Center for Neurodegenerative Diseases.

Ethics approval and consent to participate

All animal experiments were conducted in accordance with ethical animal research standards defined by the Directive 2010/63/EU, the Finnish law and the recommendations of the Finnish Ethical Committee on Animal Health and Care (license numbers: ESAVI/6105/04.10.07/2015 and ESAVI/13626/2021).

Consent for publication

All authors have approved the last version of this manuscript for publication.

Supplementary materials

Supplementary material associated with this article can be found, in the online version, at doi:10.1016/j.matbio.2024.02.007.

References

[1] J.M. Wardlaw, C. Smith, M. Dichgans, Mechanisms of sporadic cerebral small vessel disease: insights from neuroimaging, Lancet Neurol. 12 (5) (2013) 483–497.
[2] R.J. Cannistraro, et al., CNS small vessel disease: a clinical review, Neurology 92 (24) (2019) 1146–1156.
[3] S.P. Rensma, et al., Cerebral small vessel disease and risk of incident stroke, dementia and depression, and all-cause mortality: a systematic review and meta-analysis, Neurosci. Biobehav. Rev. 90 (2018) 164–173.
[4] Y.J. Kim, et al., Gray and white matter changes linking cerebral small vessel disease to gait disturbances, Neurology 86 (13) (2016) 1199–1207.
[5] M.J. Hollocks, et al., Differential relationships between apathy and depression with white matter microstructural changes and functional outcomes, Brain Pathol. 138 (12) (2015) 3803–3815.
[6] M.J. van Agtmaal, et al., Association of microvascular dysfunction with late-life depression: a systematic review and meta-analysis, JAMA Psychiatry 74 (7) (2017) 729–739.
[7] H.M. Van Der Holst, et al., Cerebral small vessel disease and incident parkinsonism: the RUN DMC study, Neurology 85 (18) (2015) 1569–1577.
[8] J.M. Wardlaw, C. Smith, M. Dichgans, Small vessel disease: mechanisms and clinical implications, Lancet Neurol. 18 (7) (2019) 684–696.
[9] A.J. Farrall, J.M. Wardlaw, Blood–brain barrier: ageing and microvascular disease–systematic review and meta-analysis, Neurobiol. Aging 30 (3) (2009) 337–352.
[10] M. Vernooij, et al., Prevalence and risk factors of cerebral microbleeds: the Rotterdam Scan Study, Neurology 70 (14) (2008) 1208–1214.
[11] J. Wardlaw, et al., Is breakdown of the blood-brain barrier responsible for lacunar stroke, leukoaraiosis, and dementia? Stroke 34 (3) (2003) 806–812.
[12] Q. Li, et al., Cerebral small vessel disease, Cell Transplant. 27 (12) (2018) 1711–1722.
[13] R.N. Kalaria, The pathology and pathophysiology of vascular dementia, Neuropharmacology 134 (2018) 226–239.
[14] S. Schreiber, et al., Invited Review: the spectrum of age-related small vessel diseases: potential overlap and interactions of amyloid and nonamyloid vasculopathies, Neuropathol. Appl. Neurobiol. 46 (3) (2020) 219–239.
[15] A. Low, et al., Inflammation and cerebral small vessel disease: a systematic review, Ageing Res. Rev. 53 (2019) 100916.
[16] K.S. Mark, D.W. Miller, Increased permeability of primary cultured brain microvessel endothelial cell monolayers following TNF-α exposure, Life Sci. 64 (21) (1999) 1941–1953.
[17] C.T. Capaldo, A.s. Nusrat, Cytokine regulation of tight junctions, Biochim. Biophys. Acta -Biomembr. 1788 (4) (2009) 864–871.
[18] A. Montagne, et al., Pericyte degeneration causes white matter dysfunction in the mouse central nervous system, Nat. Med. 24 (3) (2018) 326.
[19] E.L. Bailey, et al., Differential gene expression in multiple neurological, inflammatory and connective tissue pathways in a spontaneous model of human small vessel stroke, Neuropathol. Appl. Neurobiol. 40 (7) (2014) 855–872.
[20] E. Persyn, et al., Genome-wide association study of MRI markers of cerebral small vessel disease in 42,310 participants, Nat. Commun. 11 (1) (2020) 1–12.
[21] R. Lemmens, et al., Novel COL4A1 mutations cause cerebral small vessel disease by haploinsufficiency, Hum. Mol. Genet. 22 (2) (2013) 391–397.
[22] L.C. Rutten-Jacobs, et al., Common NOTCH3 variants and cerebral small-vessel disease, Stroke 46 (6) (2015) 1482–1487.
[23] F. Held, et al., Vascular basement membrane alterations and β-amyloid accumulations in an animal model of cerebral small vessel disease, Clin. Sci. 131 (10) (2017) 1001–1013.
[24] G.A. Rosenberg, Extracellular matrix inflammation in vascular cognitive impairment and dementia, Clin. Sci. 131 (6) (2017) 425–437.
[25] A.H. Hainsworth, H.S. Markus, Do in vivo experimental models reflect human cerebral small vessel disease? A systematic review, J. Cerebral. Blood Flow Metabol. 28 (12) (2008) 1877–1891.
[26] H. Braun, et al., Stases are associated with blood–brain barrier damage and a restricted activation of coagulation in SHRSP, Neurol. Sci. 322 (1–2) (2012) 71–76.
[27] T. Van Agtmael, Bruckner-Tuderman, Basement membranes and human disease, Cell Tissue Res. 339 (1) (2010) 167–188.
[28] A.D. Paepe, F. Malfait, Bleeding and bruising in patients with Ehlers–Danlos syndrome and other collagen vascular disorders, Br. J. Haematol. 127 (5) (2004) 491–500.
[29] M.J. Eagleton, Arterial complications of vascular Ehlers-Danlos syndrome, J. Vasc. Surg. 64 (6) (2016) 1869–1880.
[30] A.L. Sertié, et al., Collagen XVIII, containing an endogenous inhibitor of angiogenesis and tumor growth, plays a critical role in the maintenance of retinal structure and in neural tube closure (Knobloch syndrome), Hum. Mol. Genet. 9 (13) (2000) 2051–2058.
[31] O. Suzuki, et al., Molecular analysis of collagen XVIII reveals novel mutations, presence of a third isoform, and possible genetic heterogeneity in Knobloch syndrome, Am. J. Hum. Genet. 71 (6) (2002) 1320–1329.
[32] Y. Muragaki, et al., Mouse Col18a1 is expressed in a tissue-specific manner as three alternative variants and is localized in basement membrane zones, Proc. Natl. Acad. Sci. 92 (19) (1995) 8763–8767.
[33] N.K. Acharya, et al., Diabetes and hypercholesterolemia increase blood-brain barrier permeability and brain amyloid deposition: beneficial effects of the LpPLA2 inhibitor darapladib, J. Alzheimer's Dis. 35 (1) (2013) 179–198.
[34] L. Seppinen, T. Pihlajaniemi, The multiple functions of collagen XVIII in development and disease, Matrix Biol. 30 (2) (2011) 83–92.
[35] M. Monet-Leprêtre, et al., Abnormal recruitment of extracellular matrix proteins by excess Notch3ECD: a new pathomechanism in CADASIL 136 (6) (2013) 1830–1845.
[36] M. Ball, Neuronal loss, neurofibrillary tangles and granulovacuolar degeneration in the hippocampus with ageing and dementia, Acta Neuropathol. 37 (2) (1977) 111–118.
[37] A.C. Johnson, Hippocampal vascular supply and its role in vascular cognitive impairment, Stroke 54 (3) (2023) 673–685.
[38] V. Perosa, et al., Hippocampal vascular reserve associated with cognitive performance and hippocampal volume, Brain 143 (2) (2020) 622–634.
[39] D.A. Edelman, et al., Cytokine production in lipopolysaccharide-exposed rat lung pericytes, J. Trauma Acute Care Surg. 62 (1) (2007) 89–93.
[40] D. Dong, et al., VX-765 alleviates β-amyloid deposition and secondary degeneration in the ipsilateral hippocampus and ameliorates cognitive decline after focal cortical infarction in rats, J. Mol. Neurosci. 72 (12) (2022) 2389–2397.
[41] T. Koizumi, et al., Vessel-associated immune cells in cerebrovascular diseases: from perivascular macrophages to vessel-associated microglia, Front. Neurosci. (2019) 1291.
[42] W.J. Streit, et al., Dystrophic (senescent) rather than activated microglial cells are associated with tau pathology and likely precede neurodegeneration in Alzheimer's disease, Acta Neuropathol. 118 (2009) 475–485.
[43] S. Sayeed, et al., S100A10 is required for the organization of actin stress fibers and promotion of cell spreading, Mol. Cell. Biochem. 374 (2013) 105–111.
[44] L. Strackeljan, et al., Microglia depletion-induced remodeling of extracellular matrix and excitatory synapses in the hippocampus of adult mice, Cells 10 (8) (2021) 1862.

[45] É. Gervais, et al., Structural analysis of the microglia-interneuron interactions in the CA1 hippocampal area of the APP/PS1 mouse model of Alzheimer's disease, J. Comp. Neurol. (2021).
[46] M.-J. Goumans, Z. Liu, P. Ten Dijke, TGF-β signaling in vascular biology and dysfunction, Cell Res. 19 (1) (2009) 116–127.
[47] P. Ten Dijke, H.M. Arthur, Extracellular control of TGFβ signalling in vascular development and disease, Nat. Rev. Mol. Cell Biol. 8 (11) (2007) 857–869.
[48] T. Kato, et al., Excessive production of transforming growth factor β1 causes mural cell depletion from cerebral small vessels, Front. Aging Neurosci. 12 (2020) 151.
[49] Y. Yamamoto, M. Ihara, Disruption of transforming growth factor-β superfamily signaling: a shared mechanism underlying hereditary cerebral small vessel disease, Neurochem. Int. 107 (2017) 211–218.
[50] K.S. Moulton, et al., Loss of collagen XVIII enhances neovascularization and vascular permeability in atherosclerosis, Circulation 110 (10) (2004) 1330–1336.
[51] A. Blamire, et al., Interleukin-1β-induced changes in blood–brain barrier permeability, apparent diffusion coefficient, and cerebral blood volume in the rat brain: a magnetic resonance study, J. Neurosci. 20 (21) (2000) 8153–8159.
[52] N. Laflamme, S. Lacroix, S. Rivest, An essential role of interleukin-1β in mediating NF-κB activity and COX-2 transcription in cells of the blood–brain barrier in response to a systemic and localized inflammation but not during endotoxemia, J. Neurosci. 19 (24) (1999) 10923–10930.
[53] A.T. Argaw, et al., IL-1β regulates blood-brain barrier permeability via reactivation of the hypoxia-angiogenesis program, J. Immunol. 177 (8) (2006) 5574–5584.
[54] S. Jandke, et al., The association between hypertensive arteriopathy and cerebral amyloid angiopathy in spontaneously hypertensive stroke-prone rats, Brain Pathol. 28 (6) (2018) 844–859.
[55] S. Schreiber, et al., Blood brain barrier breakdown as the starting point of cerebral small vessel disease?-New insights from a rat model, Exp. Transl. Stroke Med. 5 (1) (2013) 1–8.
[56] R.M. Rajani, et al., Reversal of endothelial dysfunction reduces white matter vulnerability in cerebral small vessel disease in rats, Sci. Transl. Med. 10 (448) (2018) eaam9507.
[57] D. Graham, et al., Candidate genes that determine response to salt in the stroke-prone spontaneously hypertensive rat: congenic analysis, Hypertension 50 (6) (2007) 1134–1141.
[58] C.-W. Huang, et al., Clinical significance of circulating vascular cell adhesion molecule-1 to white matter disintegrity in Alzheimer's dementia, Thromb. Haemost. 114 (12) (2015) 1230–1240.
[59] R. Brondani, et al., Levels of vascular cell adhesion molecule-1 and endothelin-1 in ischemic stroke: a longitudinal prospective study, Clin. Biochem. 40 (3–4) (2007) 282–284.
[60] L. Badimon, G. Vilahur, Thrombosis formation on atherosclerotic lesions and plaque rupture, J. Intern. Med. 276 (6) (2014) 618–632.
[61] N. Kivinen, et al., Absence of collagen XVIII in mice causes age-related insufficiency in retinal pigment epithelium proteostasis, Biogerontology 17 (4) (2016) 749–761.
[62] T. Wyss-Coray, et al., Increased central nervous system production of extracellular matrix components and development of hydrocephalus in transgenic mice overexpressing transforming growth factor-beta 1, Am. J. Pathol. 147 (1) (1995) 53.
[63] C. Schachtrup, et al., Fibrinogen triggers astrocyte scar formation by promoting the availability of active TGF-β after vascular damage, J. Neurosci. 30 (17) (2010) 5843–5854.
[64] M. Buckwalter, et al., Molecular and functional dissection of TGF-β1-induced cerebrovascular abnormalities in transgenic mice, Ann. N. Y. Acad. Sci. 977 (1) (2002) 87–95.
[65] T. Wyss-Coray, et al., Chronic overproduction of transforming growth factor-β1 by astrocytes promotes Alzheimer's disease-like microvascular degeneration in transgenic mice, Am. J. Pathol. 156 (1) (2000) 139–150.
[66] E. Hamel, Cerebral circulation: function and dysfunction in Alzheimer's disease, J. Cardiovasc. Pharmacol. 65 (4) (2015) 317–324.
[67] W. Chen, et al., Assessment of the Virchow-Robin Spaces in Alzheimer disease, mild cognitive impairment, and normal aging, using high-field MR imaging, Am. J. Neuroradiol. 32 (8) (2011) 1490–1495.
[68] K.M. Lynch, et al., Brain perivascular space imaging across the human lifespan, Neuroimage (2023) 120009.
[69] H. Nozaki, M. Nishizawa, O. Onodera, Features of cerebral autosomal recessive arteriopathy with subcortical infarcts and leukoencephalopathy, Stroke 45 (11) (2014) 3447–3453.
[70] L. Muhl, et al., Single-cell analysis uncovers fibroblast heterogeneity and criteria for fibroblast and mural cell identification and discrimination 11 (1) (2020) 3953.
[71] J. Kyyriäinen, X.E. Ndode-Ekane, A. Pitkänen, Dynamics of PDGFRβ expression in different cell types after brain injury, Glia 65 (2) (2017) 322–341.
[72] R.E. Petrea, et al., Mid to late life hypertension trends and cerebral small vessel disease in the framingham heart study, Hypertension 76 (3) (2020) 707–714.
[73] G.L. Baumbach, D.D. Heistad, Cerebral circulation in chronic arterial hypertension, Hypertension 12 (2) (1988) 89–95.
[74] P. Martinez-Quinones, et al., Hypertension induced morphological and physiological changes in cells of the arterial wall, Am. J. Hypertens 31 (10) (2018) 1067–1078.
[75] M. Merlini, et al., Fibrinogen induces microglia-mediated spine elimination and cognitive impairment in an Alzheimer's disease model, Neuron 101 (6) (2019) 1099–1108, e6.
[76] J. Vom Berg, et al., Inhibition of IL-12/IL-23 signaling reduces Alzheimer's disease–like pathology and cognitive decline, Nat. Med. 18 (12) (2012) 1812–1819.
[77] T. Wyss-Coray, L. Mucke, Inflammation in neurodegenerative disease—A double-edged sword, Neuron 35 (3) (2002) 419–432.
[78] Y. Wang, et al., Interleukin-1β induces blood–brain barrier disruption by downregulating sonic hedgehog in astrocytes, PLoS ONE 9 (10) (2014) e110024.
[79] J.D. Cherry, et al., CCL2 is associated with microglia and macrophage recruitment in chronic traumatic encephalopathy, J. Neuroinflamm. 17 (1) (2020) 1–12.
[80] N.P. Rudemiller, S.D. Crowley, The role of chemokines in hypertension and consequent target organ damage, Pharmacol. Res. 119 (2017) 404–411.
[81] A. Nimmerjahn, F. Kirchhoff, F. Helmchen, Resting microglial cells are highly dynamic surveillants of brain parenchyma in vivo, Sci. Transl. Med. 308 (5726) (2005) 1314–1318.
[82] M.E. Benoit, et al., C1q-induced LRP1B and GPR6 proteins expressed early in Alzheimer disease mouse models, are essential for the C1q-mediated protection against amyloid-β neurotoxicity, J. Biol. Chem. 288 (1) (2013) 654–665.
[83] Y. Okuzono, et al., Reduced TREM2 activation in microglia of patients with Alzheimer's disease, FEBS Open Bio 11 (11) (2021) 3063–3080.
[84] T. Jiang, et al., Upregulation of TREM2 ameliorates neuropathology and rescues spatial cognitive impairment in a transgenic mouse model of Alzheimer's disease, Neuropsychopharmacology 39 (13) (2014) 2949–2962.
[85] C.D. Lee, et al., Elevated TREM2 gene dosage reprograms microglia responsivity and ameliorates pathological phenotypes in Alzheimer's disease models, Neuron 97 (5) (2018) 1032–1048, e5.
[86] S.A. Liddelow, et al., Neurotoxic reactive astrocytes are induced by activated microglia, Nature 541 (7638) (2017) 481–487.
[87] A. Fujita, et al., Connexin 30 deficiency attenuates A2 astrocyte responses and induces severe neurodegeneration in a1-methyl-4-phenyl-1, 2, 3, 6-tetrahydro-pyridine hydrochloride Parkinson's disease animal model, J. Neuroinflammation 15 (1) (2018) 1–20.
[88] H. Hayani, I. Song, A. Dityatev, Increased excitability and reduced excitatory synaptic input into fast-spiking CA2 interneurons after enzymatic attenuation of extracellular matrix, Front. Cell. Neurosci. 12 (2018) 149.
[89] S. Lemarchant, et al., ADAMTS-4 promotes neurodegeneration in a mouse model of amyotrophic lateral sclerosis, Mol. Neurodegener. 11 (1) (2016) 1–24.
[90] K. Satoh, N. Suzuki, H. Yokota, ADAMTS-4 (a disintegrin and metalloproteinase with thrombospondin motifs) is transcriptionally induced in beta-amyloid treated rat astrocytes, Neurosci. Lett. 289 (3) (2000) 177–180.
[91] J.R. Lowry, A. Klegeris, Emerging roles of microglial cathepsins in neurodegenerative disease, Brain Res. Bull. 139 (2018) 144–156.
[92] H. Nakanishi, Microglial functions and proteases, Mol. Neurobiol. 27 (2003) 163–176.
[93] G.A. Rosenberg, Extracellular matrix inflammation in vascular cognitive impairment and dementia, J. Clin. Sci. 131 (6) (2017) 425–437.
[94] M.J. Végh, et al., Reducing hippocampal extracellular matrix reverses early memory deficits in a mouse model of Alzheimer's disease, Acta Neuropathol. Commun. 2 (1) (2014) 1–11.
[95] M. Morawski, et al., Tenascin-R promotes assembly of the extracellular matrix of perineuronal nets via clustering of aggrecan, Philos. Trans. R. Soc. B: Biol. Sci. 369 (1654) (2014) 20140046.
[96] C. Capone, et al., Reducing Timp3 or vitronectin ameliorates disease manifestations in CADASIL mice, Ann. Neurol. 79 (3) (2016) 387–403.
[97] A.C. Yang, et al., A human brain vascular atlas reveals diverse mediators of Alzheimer's risk, Nature 603 (7903) (2022) 885–892.
[98] S. Kirvell, et al., Vesicular glutamate transporter and cognition in stroke: a case-control autopsy study, Neurology 75 (20) (2010) 1803–1809.
[99] S.L. Kirvell, M. Esiri, P.T. Francis, Down-regulation of vesicular glutamate transporters precedes cell loss and pathology in Alzheimer's disease, J. Neurochem. 98 (3) (2006) 939–950.
[100] A. Kashani, et al., Loss of VGLUT1 and VGLUT2 in the prefrontal cortex is correlated with cognitive decline in Alzheimer disease, Neurobiol. Aging 29 (11) (2008) 1619–1630.
[101] S.T. DeKosky, S.W. Scheff, Synapse loss in frontal cortex biopsies in Alzheimer's disease: correlation with cognitive severity, Ann. Neurol. 27 (5) (1990) 457–464.
[102] Z. Tucsek, et al., Hypertension-induced synapse loss and impairment in synaptic plasticity in the mouse hippocampus mimics the aging phenotype: implications for the pathogenesis of vascular cognitive impairment, Geroscience 39 (2017) 385–406.
[103] I.L. Llorente, et al., Age and meloxicam modify the response of the glutamate vesicular transporters (VGLUTs) after transient global cerebral ischemia in the rat brain, Brain Res. Bull. 94 (2013) 90–97.
[104] R.A. Asher, et al., Neurocan is upregulated in injured brain and in cytokine-treated astrocytes, J. Neurosci. 20 (7) (2000) 2427–2438.
[105] B.T. Susarla, et al., Smad proteins differentially regulate transforming growth factor-β-mediated induction of chondroitin sulfate proteoglycans, J. Neurochem. 119 (4) (2011) 868–878.
[106] N. Jahan, S.S. Hannila, Transforming growth factor β-induced expression of chondroitin sulfate proteoglycans is mediated through non-Smad signaling pathways, Exp. Neurol. 263 (2015) 372–384.
[107] S.O. Park, et al., Real-time imaging of de novo arteriovenous malformation in a mouse model of hereditary hemorrhagic telangiectasia, J. Clin. Investig. 119 (11) (2009) 3487–3496.
[108] H.-L. Nguyen, et al., TGF-β signaling in endothelial cells, but not neuroepithelial cells, is essential for cerebral vascular development, Lab. Investig. 91 (11) (2011) 1554–1563.

[109] L. Maddaluno, et al., EndMT contributes to the onset and progression of cerebral cavernous malformations, Nature 498 (7455) (2013) 492–496.
[110] P.T. Ronaldson, et al., Transforming growth factor-β signaling alters substrate permeability and tight junction protein expression at the blood-brain barrier during inflammatory pain, J. Cerebr. Blood Flow Metabol. 29 (6) (2009) 1084–1098.
[111] J.M. Lawrence, et al., Roles of neuropathology-associated reactive astrocytes: a systematic review, Acta Neuropathol Commun. 11 (1) (2023) 1–28.
[112] V.V. Senatorov Jr, et al., Blood-brain barrier dysfunction in aging induces hyperactivation of TGFβ signaling and chronic yet reversible neural dysfunction, Sci. Transl. Med. 11 (521) (2019) eaaw8283.
[113] J. Liu, et al., Associated genetic variants and potential pathogenic mechanisms of brain arteriovenous malformation, J. NeuroInterven. Surg. (2022).
[114] B. Yılmaz, et al., Familial occurrence of brain arteriovenous malformation: a novel ACVRL1 mutation detected by whole exome sequencing, J. Neurosurg. 126 (6) (2016) 1879–1883.
[115] L. Grand Moursel, et al., TGFβ pathway deregulation and abnormal phospho-SMAD2/3 staining in hereditary cerebral hemorrhage with amyloidosis-Dutch type, Brain Pathology 28 (4) (2018) 495–506.
[116] M.A. McMillin, et al., TGFβ1 exacerbates blood–brain barrier permeability in a mouse model of hepatic encephalopathy via upregulation of MMP9 and downregulation of claudin-5, Lab. Investig. 95 (8) (2015) 903–913.
[117] S. Huang, et al., *The role of Smad2 and Smad3 in regulating homeostatic functions of fibroblasts* in vitro *and in adult mice*, Biochim. Biophys. Acta (BBA)-Mol. Cell Res. 1867 (7) (2020) 118703.
[118] N. Fukai, et al., Lack of collagen XVIII/endostatin results in eye abnormalities, EMBO J. 21 (7) (2002) 1535–1544.
[119] R. Carare, et al., Solutes, but not cells, drain from the brain parenchyma along basement membranes of capillaries and arteries: significance for cerebral amyloid angiopathy and neuroimmunology, Neuropathol. Appl. Neurobiol. 34 (2) (2008) 131–144.
[120] M.S. Ventura Ferreira, et al., Comprehensive characterization of chorionic villi-derived mesenchymal stromal cells from human placenta, Stem Cell Res. Ther. 9 (1) (2018) 1–17.
[121] M. Meldgaard, et al., Validation of two reference genes for mRNA level studies of murine disease models in neurobiology, J. Neurosci. Methods 156 (1–2) (2006) 101–110.
[122] R. Kaushik, et al., Traditional Japanese herbal medicine Yokukansan targets distinct but overlapping mechanisms in aged mice and in the 5xFAD mouse model of Alzheimer's disease, Front. Aging Neurosci. 10 (2018) 411.
[123] J. Schindelin, et al., Fiji: an open-source platform for biological-image analysis, Nat. Methods 9 (7) (2012) 676–682.
[124] J. Glenn, et al., Characterisation of ramified microglial cells: detailed morphology, morphological plasticity and proliferative capability, J. Anat. 180 (Pt 1) (1992) 109.
[125] I.B. Hovens, C. Nyakas, R.G. Schoemaker, A novel method for evaluating microglial activation using ionized calcium-binding adaptor protein-1 staining: cell body to cell size ratio, Neuroimmunol. Neuroinflammation 1 (2014) 82–88.
[126] E.M. York, et al., 3DMorph automatic analysis of microglial morphology in three dimensions from ex vivo and in vivo imaging, eNeuro 5 (6) (2018).
[127] C. Nolte, et al., GFAP promoter-controlled EGFP-expressing transgenic mice: a tool to visualize astrocytes and astrogliosis in living brain tissue, Glia 33 (1) (2001) 72–86.
[128] G. Matuszko, et al., Extracellular matrix alterations in the ketamine model of schizophrenia, Neurosci. Biobehav. Rev. 350 (2017) 13–22.
[129] R. Valtola, et al., VEGFR-3 and its ligand VEGF-C are associated with angiogenesis in breast cancer, Am. J. Pathol. 154 (5) (1999) 1381–1390.
[130] C.I. Seidenbecher, et al., Brevican, a chondroitin sulfate proteoglycan of rat brain, occurs as secreted and cell surface glycosylphosphatidylinositol-anchored isoforms, J. Biol. Chem. 270 (45) (1995) 27206–27212.